COMPREHENSIVE MODELING OF HEAT AND MASS TRANSPORT IN A MICROPILLAR EVAPORATOR

A THESIS SUBMITTED TO
THE GRADUATE SCHOOL OF NATURAL AND APPLIED SCIENCES
OF
MIDDLE EAST TECHNICAL UNIVERSITY

BY

GÖKSEL YUNCU

IN PARTIAL FULFILLMENT OF THE REQUIREMENTS
FOR
THE DEGREE OF MASTER OF SCIENCE
IN
MECHANICAL ENGINEERING

APRIL 2022

Approval of the thesis:

COMPREHENSIVE MODELING OF HEAT AND MASS TRANSPORT IN A MICROPILLAR EVAPORATOR

submitted by **GÖKSEL YUNCU** in partial fulfillment of the requirements for the degree of **Master of Science in Mechanical Engineering Department, Middle East Technical University** by,

Prof. Dr. Halil Kalıpçılar
Dean, Graduate School of **Natural and Applied Sciences** _____

Prof. Dr. M. A. Sahir Arıkan
Head of Department, **Mechanical Engineering** _____

Prof. Dr. Zafer Dursunkaya
Supervisor, **Mechanical Engineering, METU** _____

Assoc. Prof. Dr. Yiğit Akkuş
Co-supervisor, **Mechanical Engineering, ASELSAN** _____

Examining Committee Members:

Assoc. Prof. Dr. Cüneyt Sert
Mechanical Engineering, METU _____

Prof. Dr. Zafer Dursunkaya
Mechanical Engineering, METU _____

Assoc. Prof. Dr. Özgür Bayer
Mechanical Engineering, METU _____

Assist. Prof. Dr. Altuğ Özçelikkale
Mechanical Engineering, METU _____

Assoc. Prof. Dr. Barbaros Çetin
Mechanical Engineering, Bilkent University _____

Date: 05.04.2022

I hereby declare that all information in this document has been obtained and presented in accordance with academic rules and ethical conduct. I also declare that, as required by these rules and conduct, I have fully cited and referenced all material and results that are not original to this work.

Name, Surname: Göksel Yuncu

Signature :

ABSTRACT

COMPREHENSIVE MODELING OF HEAT AND MASS TRANSPORT IN A MICROPILLAR EVAPORATOR

Yuncu, Göksel
M.S., Department of Mechanical Engineering
Supervisor: Prof. Dr. Zafer Dursunkaya
Co-Supervisor: Assoc. Prof. Dr. Yiğit Akkuş

April 2022, 57 pages

Thin-film evaporation and the replenishing capillary liquid flow have paramount importance for various technological applications spanning from desalination to electronics cooling. With the developments enabling precise fabrication, evaporators with micropillar arrays have attracted substantial attention to sustain efficient evaporation fed by passive liquid transport. Although considerable effort has been devoted to designing optimized wicks, the full picture is still blurry due to complexities in modeling the liquid-vapor interface and the flow around the micropillars. Fundamentally, the heat transfer from a micropillar wick evaporator is a problem governed by various interfacial phenomena such as the capillarity-induced liquid flow, thin-film evaporation intensifying near the contact lines, and thermocapillarity-induced Marangoni flow. In this work, a comprehensive model is developed for the evaporation from a micropillar wick evaporator by coupling liquid flow and energy transport at both cell- and device- levels. The model is successfully validated with previous experiments. When Marangoni number is sufficiently high, the model identifies a sharp reduction in the evaporator temperature attributed to the thermocapillary convection

creating circulations beneath the liquid-vapor interface. This temperature drop cannot be identified when thermocapillarity is switched off in the model and the prediction of the model substantially deviates from the experimental measurement. Therefore, the current study reveals a hitherto unexplored role of Marangoni flow in the evaporation of water from micropillar wick evaporators. The proposal modeling framework can guide engineers to optimize micro-post evaporators by accounting for all the relevant interfacial phenomena.

Keywords: thin-film evaporation, capillary flow, Marangoni flow, micropillar wick, dryout heat flux.

ÖZ

MİKROSÜTUNLU BİR BUHARLAŞTIRICIDA ISI VE KİTLE TAŞINMASININ KAPSAMLI MODELLENMESİ

Yuncu, Göksel
Yüksek Lisans, Makina Mühendisliği Bölümü
Tez Yöneticisi: Prof. Dr. Zafer Dursunkaya
Ortak Tez Yöneticisi: Doç. Dr. Yiğit Akkuş

Nisan 2022 , 57 sayfa

İnce film buharlaşması ve kılcal sıvı akışı, tuz arındırmadan elektronik soğutmaya kadar birçok teknolojik uygulama için büyük öneme sahiptir. Hassas üretimi mümkün kılan gelişmeler sayesinde, pasif sıvı taşınımı ile beslenen mikrosütunlu buharlaştırıcılar büyük ilgi görmeye başladı. Günümüze kadar kılcal tasarımların optimize edilmesi için önemli çabalar harcanmış olsa da, sıvı-buhar arayüzündeki ve mikrosütunların etrafındaki akışta meydana gelen karmaşıklıklar sebebiyle konunun tamamı net bir şekilde anlaşılamamaktadır. Temel olarak, mikrosütunlu bir kılcal buharlaştırıcıdaki ısı transferi; kılcallık kaynaklı sıvı akışı, temas çizgisinin yakınında yoğunlaşan ince film buharlaşması ve termokapilerite kaynaklı Marangoni akışı gibi çeşitli arayüz fenomenlerini içeren bir problemdir. Bu çalışmada, sıvı akışı hücre ve cihaz seviyesinde enerji transferi ile birleştirilerek mikrosütunlu kılcal buharlaştırıcılardan buharlaşma için kapsamlı bir model geliştirilmiştir. Geliştirilen model literatürdeki önceki deneylerle başarıyla doğrulanmıştır. Marangoni sayısı yeterince yüksek olduğunda, termokapiler konveksiyon nedeniyle sıvı-buhar arayüzünün altında sirkülasyon oluştuğu,

ve bu akışın buharlaştırıcı sıcaklığını önemli derecede düşürdüğü tespit edilmiştir. Bu sıcaklık düşüşü, modelde termokapilerik fizik yok sayıldığında tanımlanamamakta ve modelin tahmini deneylerden önemli ölçüde sapmaktadır. Bu yüzden, mevcut çalışma mikrosütunlu kılcal buharlaştırıcılarda Marangoni akışının buharlaşma üzerinde şimdiye kadar keşfedilmemiş etkisini ortaya çıkarmaktadır. Önerilen modelleme yapısının, tüm arayüz fenomenlerini hesaba kattığı için mikro yapılı buharlaştırıcıların optimizasyonu için mühendislere yol göstereceğine inanılmaktadır.

Anahtar Kelimeler: ince film buharlaşması, kapiler akış, Marangoni akışı, mikrosütun kılcal hareketi, kuruma ısı akısı

To individuals who sacrifice their lives for the people they never met.

ACKNOWLEDGMENTS

I would like to express my deepest gratitude to my advisor Prof. Dr. Zafer Dursunkaya and my co-advisor Assoc. Prof. Dr. Yiğit Akkuş for their continuous support, their vision that advancing the study and for sharing their outstanding knowledge with me. Without their constructive and precious comments, this thesis study could not be completed. It was really privilege for me to study under their guidance.

Also, I want to specially thank to my co-advisor Assoc. Prof. Dr. Yiğit Akkuş for his generous and the kindest attitude towards me during our both technical and non-technical conversations. The time I spent with him was always productive and valuable for me.

I wish to express my appreciation to my colleagues at ASELSAN INC. and friends at METU for supporting and motivating me during my thesis studies. I would like to thank the support from the BIDEB 2210-A program.

Lastly but most importantly, I would like to express gratefulness from the deep inside of my heart to my parents Aysel Yuncu and Gökhan Yuncu, and my brother Barış Yuncu for their contributions, their encourage and support at every moment of my life. These accomplishments would not have been possible without them.

TABLE OF CONTENTS

LIST OF TABLES

TABLES

LIST OF FIGURES

FIGURES

LIST OF ABBREVIATIONS

2-D	2 Dimensional
3-D	3 Dimensional
A_c	Cross sectional area, m^2
c_p	Specific heat capacity, J/(kg·K)
d	Pillar diameter, m
h	Pillar height, m
H	Surface height, m
h_{eff}	Effective heat transfer coefficient, W/(m^2·K)
h_{int}	Interfacial heat transfer coefficient, W/(m^2·K)
h_{fg}	Latent heat of evaporation, J/kg
k	Thermal conductivity, W/(m·K)
l	Pitch, m
L	Total wick length, m
L_t	Tangential meniscus length, m
$\dot{m}$	Mass flow rate, kg/s
$\dot{m}_e$	Evaporator mass flow rate, kg/s
$\dot{m}_{tot}$	Total mass flow rate, kg/s
$\dot{m}''_{evap}$	Evaporative mass flux , kg/m^2·s
M	Molar mass of the liquid, kg/mol
Ma	Marangoni number, -
MAC	Mass accommodation coefficient, -
$\hat{n}$	Unit normal vector, -
p_c	Capillary pressure, Pa
p_l	Liquid pressure, Pa

p_v	Vapor pressure, Pa
$q^{''}$	Heat flux, W/m^2
q''_{dryout}	Dryout heat flux, W/m^2
q''_e	Evaporator heat flux, W/m^2
q''_{in}	Applied heat flux, W/m^2
R_u	Universal gas constant, J/mol·K
$\hat{t}$	Unit tangential vector, -
t_s	Base substrate thickness, m
T	Temperature, K
$T_{e,a}$	Average evaporator temperature, K
u	Velocity in x-direction, m/s
$\overline{U}$	Average velocity in the wicking direction, m/s
	Greek Symbols
α	Thermal diffusivity of liquid, m^2/s
ΔT	Evaporator superheat, K
θ	Contact angle, Radian
κ	Permeability, 1/m^2
μ	Dynamic viscosity, Pa·s
ν	Kinematic viscosity, m^2/s
ρ	Density, kg/m^3
σ	Surface tension, N/m
$\hat{\sigma}$	Mass accommodation coefficient, -
	Subscripts
av	Average
$dryout$	Dryout
$evap$	Evaporation
e	Evaporator

env	Environment
in	Inlet
int	Interface
l	Liquid
lv	Liquid-vapor
out	Outlet
rec	Receding
sat	Saturation
s	Substrate
tot	Total
v	Vapor

CHAPTER 1

INTRODUCTION

1.1 Motivation

Over the past decades, drastic increases have arisen in the amount of energy consumption of electronic devices, as expectations from technology have increased despite the reduced size of technological devices that affect the fate of humanity. Ceramic-based GaN (Gallium nitride) chips, microprocessors, high-frequency power amplifiers, and LTCC (low temperature co-fired ceramics) modules employed in the shrinking electronic devices are exposed to exponentially diminishing efficiencies and reduced lifespan with excessive operating temperatures. Consequently, thermal maintenance becomes crucial to increase the processors efficiencies and achieve sensible operating hours. Since high heat dissipation occurs in small area, keeping operating temperature at a reasonable level for high power density electronic instruments is not possible with conventional cooling methods. Spreading the excessive heat from the hotspots to a broader area through minimum thermal resistance, then removing the dissipated heat from the system with conventional methods is feasible. Phase-change heat spreading devices (vapor chambers, heat pipes, etc.) that utilize high liquid-vapor latent heat are remarked to spread high-density heat flux with a relatively low-temperature variation. Although the active boiling methods can meet very high heat fluxes, they require high energy to operate and are unstable due to the nature of the boiling. On the other hand, passive pillar-shaped phase-change devices are stable, and their performance is predictable. There is an opening area of research to thoroughly assess evaporator physics to predict the wick structure's performance and optimize the configuration to meet the system requirements.

1.2 Background

Continuous improvements in semi-conductor fabrication techniques have opened up an avenue for the production of integrated circuits with increasing computational power in the past decades. While the decrease of feature size on a 2-D chip had determined the performance in conjunction with Moore's law [1]; currently, in the post-Moore era, performance is still enhanced by stacking 3-D chips vertically. Yet, all this progress comes with an inevitable cost: excessive heat fluxes. Specifically, excessive local heat fluxes (*e.g.* power amplifier hot spots exceeding 10 $\mathrm{kW\,cm^{-2}}$ [2]) create severe thermal challenges, which cannot be handled by traditional approaches. These hot spots may be actively cooled down *in situ* by intra-chip liquid circulation by establishing proper microfluidics-based solutions [2]. When intra-chip active liquid cooling cannot be established, the heat from the hot spots should be transported to a broader heat removal area with a sufficiently small thermal resistance to eliminate the excessive temperature rise.

When conduction is the sole heat transport mechanism, thermal resistance is determined by the thermal conductivity of the solid, which is inadequate to materialize the desired resistance values. This issue can be overcome by two-phase heat spreaders using the liquid-vapor phase change as the energy transport mechanism. The bottleneck in the design of two-phase heat spreaders is the evaporator due to the need for removing localized heat inputs of excessively large magnitudes without any dryout. The design success is determined based on the optimization of the wick structure, which should provide sufficient liquid pumping together with minimum film resistance. A thorough optimization demands control over both the design parameters and fabrication. Owing to the advances in micro and nano fabrication techniques, the high-resolution control of surface topography over length scales ranging from molecular-level to macro-level becomes possible, which allows numerous opportunities for the heat transfer enhancement *via* varying scale surface structures [3–5]. As opposed to the coating-based methods (*e.g.* nanowire coating, CNT coating, *etc.*), which, in general, generate a random distribution of surface features, lithography-based methods are able to create features (*e.g.* micro-scale and nano-scale posts, *etc.*) with exact shapes and sizes. Accordingly, thin-film evaporation from these engineered surfaces

has gained substantial attention in recent decades.

Evaporators with micro-scale posts (commonly referred to as micropillars) have been extensively studied both experimentally [6–8] and numerically [9–11]. Cylindrical micropillars attracted substantial attention among the different shaped micro-post evaporators due to their superior capillary pressure and permeability performance compared to their polygon-shaped counterparts with sharp corners [9]. The performance of an evaporator is assessed by the maximum dryout heat flux and the effective thermal resistance of the wick structure [12]. While the maximum dryout heat flux is proportional to the capillary pressure and permeability, thermal resistance scales go down with interfacial area and up with film thickness. Therefore, accurate prediction of permeability, capillary pressure, and thermal resistance is essential for exploiting the full potential of an evaporator.

Many prior studies focused on the modeling of capillary liquid flow through micropillar arrays without thermal considerations. A common simplification was to assume a 2-D liquid flow through square and hexagonal packed arrays of infinitely long micropillars [13–17]. The effect of interfacial geometry (*i.e.* 3-D meniscus shape) was also negated in previous capillary flow models [18–20]. These models primarily characterized the flow in terms of effective porosity and permeability that were obtained *via* Darcy's law [15–18] or Brinkman equation [19, 20].

Because of its 3-D nature, the meniscus-shaped liquid-vapor interface established between the pillars requires attention. Surface Evolver [21] enables obtaining 3-D interfacial geometries based on the surface energy minimization principle. Many studies [7–9, 22, 23] utilized Surface Evolver to generate the interfacial geometry *a priori*. They then calculated the permeability and thermal resistance accordingly as inputs for the numerical simulations. These studies revealed that the increase in interface curvature enhances the evaporation flux by widening the thin-film region, whereas it deteriorates the liquid flow by reducing the wick permeability due to decreasing flow area [9, 22]. The accuracy of different permeability models [8, 9, 15, 16, 23–27] is experimentally and theoretically assessed on four different wick structures by Ravi *et al.* [10]. They suggested a unified model that can predict the mass transfer with an error less than 18% by combining the capillarity model of [8] and the permeability

model of [23]. For a better prediction of dryout heat flux, Zhu *et al.* [11] developed a model by considering the variation of the meniscus shape with capillary pressure and local permeability. They also conducted validation studies by experimenting with evaporation into the air atmosphere and reported the optimal wick geometry for the maximum dryout heat flux as functions of pillar diameter (d), height (h), and the pitch (l) as follows: $d/h \sim 0.4 - 0.6$ and $l/d \sim 3.0$.

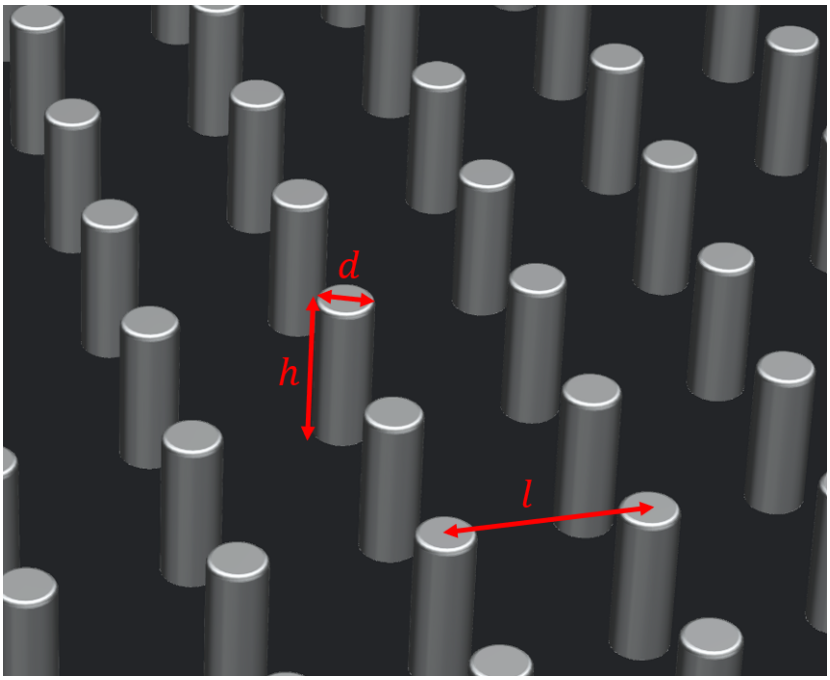

Figure 1.1: Three-dimensional representation of pillar array wick structure, where d is pillar diameter, l is pitch, and h is pillar height.

In addition to the studies targeting the prediction of dryout heat load, there were other studies [9, 28–32] that focused on the estimation of interfacial heat flux by considering the thin-film evaporation and/or applying kinetic theory based evaporation models. Ranjan *et al.* [28] investigated the wicking performance and effective thermal resistance for commonly used topologies as a function of a non-dimensional number that defines the characteristics of microstructures, liquid filling volume, and the contact angle. Farokhnia *et al.* [30] conducted theoretical and experimental studies to systematically optimize interfacial heat flux for rectangular ribs, vertical circular, and square pillar configurations. They determined evaporative mass flux at the interface using Hertz-Knudsen equation and suggested an optimum pitch-to-diameter

ratio, $l/d \sim 1.8$, to maximize the heat flux by thin-film evaporation. Recently, Bongarala *et al.* [32] developed a non-dimensional metric (a figure of merit) to evaluate the evaporative heat flux for several wick structures and compared their predictions with those in previous studies [9, 29–31].

More comprehensive models were developed by coupling the fluid flow and thermal models to investigate the evaporation from cylindrical micropillars. Adera *et al.* [33] investigated the effect of porosity and pillar height for the optimum wick design to maximize the evaporation performance. They predicted the dryout heat flux based on a semi-analytical model similar to that of [23] and estimated the interfacial thermal resistance using Schrage equation [34]. The authors employed invariant permeability and thermal resistance values at the receding contact angle for the entire domain and neglected the curvature variation along the wicking direction. They also conducted verification experiments under a controlled environment sustaining steady evaporation into pure vapor and validated their model with 20% accuracy. Wei *et al.* [35] carried out a parametric investigation to optimize the wick design by conducting a wide range of experiments using varying micropillar geometries. In addition, the authors assessed their experimental results, specifically dryout heat flux and superheat, based on previous modeling efforts [10]. Somasundaram *et al.* [36] compared the accuracy of existing permeability models and provided guidance for the optimal design to maximize dryout heat flux and minimize thermal resistance simultaneously. Recently, Vaarstra *et al.* [12] developed a comprehensive model to apprehend arbitrary thermal load and non-uniform evaporation by extending the permeability model of [11]. Their model accurately calculates the variation of the capillary pressure, heat transfer coefficient and temperature distribution along the substrate.

Fundamentally, the heat transfer from a micropillar wick evaporator is a problem governed by various interfacial phenomena such as the capillarity induced liquid flow and thin-film evaporation intensifying near the contact lines. Thermocapillarity is also a well-known mechanism, which induces a surface flow (commonly known as Marangoni flow) on non-isothermal interfaces. Its significant contribution to the convective transport, and the heat transfer thereof, was experimentally and theoretically demonstrated in different systems such as the evaporation of water droplets [37–39]. However, the role of Marangoni convection in the micropillar wick evaporators has

been overlooked mostly due to the complexity of the modeling for this problem. In fact, there were early modeling efforts to assess the effect of Marangoni flow in micropillar wicks [9, 29]. However, these attempts were not able to address the true effect of thermocapillarity since the transport mechanisms were handled only at the cell-level, which prevented exploring its impact on the capillary flow along the substrate, and the overall thermal performance thereof.

The present study aims to build a comprehensive model for the simultaneous prediction of dryout heat flux and local temperature distribution for a micropillar wick evaporator. In this study, the permeability and thermal model developed in [11, 12] is extended to capture the effect of thermocapillarity induced Marangoni convection in the cell-level model. The effect of Marangoni convection is then reflected on the device-level model in terms of permeability and effective thermal resistance for evaporation. The current model is validated with three controlled sets of distinct experiments to exhibit the model's capabilities in predicting dryout heat flux, heat transfer coefficient, and the effect of Marangoni flow. After ensuring the model's accuracy, a representative optimization study is conducted to guide the engineers in designing the micropillar evaporator, and the importance of Marangoni convection is revealed in this study.

1.3 Thesis objective and outline

In order to predict thin film evaporation in micropillars, a vast number of different numerical and semi-analytical models have been developed, and many experiments have been conducted in controlled environments to understand the basics of wicking and evaporation through the meniscus. Numerous parameters influence the performance of the wick structure (diameter, pitch, height, contact angle, etc.), and 3-D complex physics are involved in passive capillary wicking and thin-film evaporation. Therefore, simplified models can be misleading due to the assumptions made and neglected complex physics. The approach in this thesis aims to develop a comprehensive model that can capture the complex physics in heat transfer and capillary wicking, and to guide engineers for the design with this developed model. The structure and the contributions of this thesis are explained as follows:

In Chapter 1, the purpose of advanced thermal management techniques and the advantage of passive liquid-vapor phase change devices over different wick structures are discussed. After a brief review of the literature for various modeling approaches, a framework that addresses maximum heat flux, temperature variation, and the effect of the thermocapillary flow on the design of the wick structure is proposed.

In Chapter 2, the comprehensive model is explained in detail, and the capabilities of the developed model are described at the cell-level and device-level models.

In Chapter 3, the current model's ability to predict two performance criteria (dryout heat flux, evaporator superheat) is verified with three distinct sets of experiments. Also, the effect of Marangoni convection on the dryout heat flux and heat transfer coefficient is investigated.

In Chapter 4, the effect of the wick structure and the pillar ratios (l/d, d/h) on the performance of evaporator is investigated. In addition, an optimization study for hypothetical but realistic thermal requirements is conducted to guide engineers for evaporator design. Also, the effect of the thermocapillary model on the results with the design conditions at which it should be taken into account is discussed.

In Chapter 5, the results of the current study are concluded, recommendations about future work and extensible research with the proposed model are discussed.

CHAPTER 2

MODELING METHODOLOGY

This study investigates evaporation from regularly packed pillar arrays at the micro (cell-level), and macro (device-level) scales to obtain sufficiently accurate results with a low computational cost. At the cell-level, numerous cell-level simulations are conducted at different contact angles and evaporative heat fluxes (q''_e) to create look-up tables for permeability (κ) and effective heat transfer coefficient (h_{eff}) that are employed in the device-level evaporator model. At the device-level, variable heat flux $q''_{in}(x)$ is applied at the bottom surface of the substrate with a thickness of t_s. The energy and liquid transport are coupled through the device-level flow and conduction models. The computational model utilizes temperature-dependent properties which are taken from the material library of COMSOL Multiphysics software [42].

Parametric studies are performed at the cell level for a wide range of geometries and contact angles to obtain curvature-dependent permeability (κ) and effective heat transfer coefficient (h_{eff}) as a function of geometry and capillary pressure. Then curvature-dependent local permeability and heat transfer coefficient values are utilized in the discretized device-level conduction model. All cells are linked to satisfy the conservation of mass, momentum, and energy throughout the substrate by coupling the energy and fluid transport problems. The dryout heat flux and spatially varying evaporative superheat for any geometry can be predicted accurately. The model can solve the unidirectional and bidirectional flow, resolve arbitrary thermal loads and determine the importance of the thermocapillary effect for a given geometry and heat flux input.

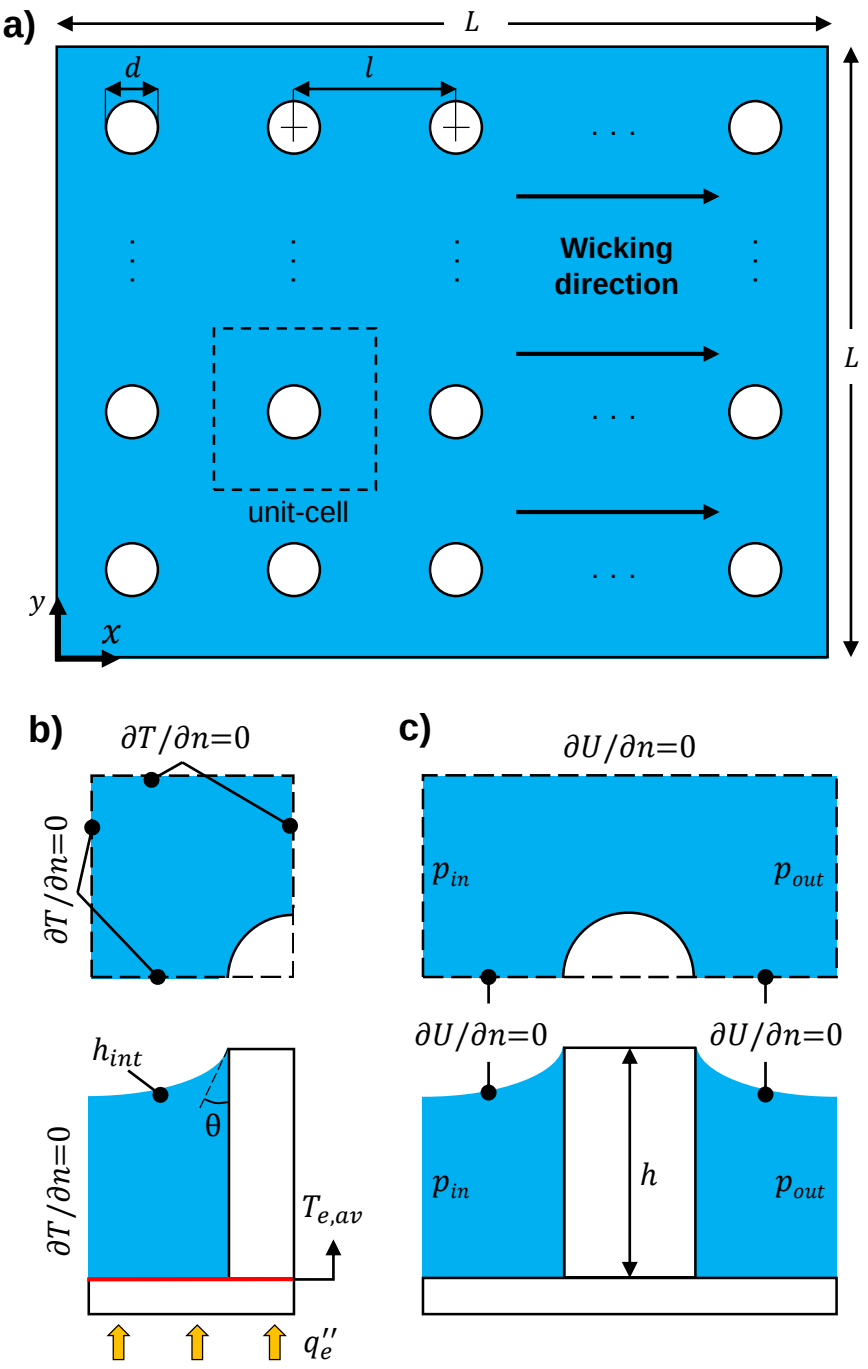

Figure 2.1: **a)** Top view of the evaporator. The pillar array dimensions are d, l, h, and L, where d is diameter, l is pitch, h is height, L is the total wicking length. **b)** Top and front view of the quarter unit-cell and boundary conditions for the heat transfer problem. θ is the angle between solid-liquid contact at the pillar edge. **c)** Top and front view of the half unit-cell and boundary conditions for the flow problem.

2.1 Cell-level Model

In the cell-level model, permeability and effective heat transfer coefficient are obtained in unit-cells with different contact angles, then they are utilized in the discretized device-level model to capture the variation of permeability and effective heat transfer coefficient in the wicking direction. Initially, 3-D meniscus shapes at various contact angles are generated (Sec. 2.1.1). Then the generated 3-D geometries are employed as the computational domain for cell-level energy (Sec. 2.1.2) and liquid (Sec. 2.1.3) transport problems together with the thermocapillarity induced flow problem (Sec. 2.1.4). The mesh independence study for cell-level models is presented in Appendix A.1.

2.1.1 Meniscus Shape

In this study, the variation of the pressure and curvature within a cell is negligible ($l \ll L$), and the disjoining pressure is negligible for the geometries (1-90 μm) studied. Three-dimensional meniscus shape formed between the pillars is a function of the local liquid and vapor pressures. Assuming negligible variation of the vapor pressure, capillary pressure, p_c, is defined as the local liquid-vapor pressure difference $p_c(x) = p_v - p_l(x)$ that is given by the Young-Laplace (Y-L) equation:

$$\nabla \cdot \hat{n} = p_c(x)/\sigma \tag{2.1}$$

where σ is surface tension, and $\hat{n}$ is the outward unit normal of the surface. Surface tension values between the liquid and vapor phases are taken from the library of COMSOL Multiphysics software [42]. The shape of interface is denoted as a geometric function of the surface height, H, and the unit outward normal of the interface is defined as follows:

$$\hat{n} = \frac{(H_x, H_y, -1)}{(H_x^2 + H_y^2 + 1)^{1/2}} \tag{2.2}$$

where subscripts x and y represents the derivatives in the corresponding directions.

After substituting Equation (2.2) into Y-L equation, appropriate boundary conditions are needed to solve this nonlinear differential equation. By taking advantage of the symmetries within a unit-cell, only a quarter of the unit-cell is defined as the problem domain (Figure 2.1b). The three-phase contact line is fully pinned to the pillar top (z=0), and the other boundary conditions are defined as symmetry conditions.

The Y-L equation is solved to obtain height expression of the interface shape for a given capillary pressure, and the expression is utilized to form the 3-D deformed meniscus shape. A sample Y-L equation solution and the deformed 3-D meniscus according to this result are shown in Figure 2.2. The generated 3-D liquid domains serve as the simulation domain for liquid and energy transport problems in the cell-level model.

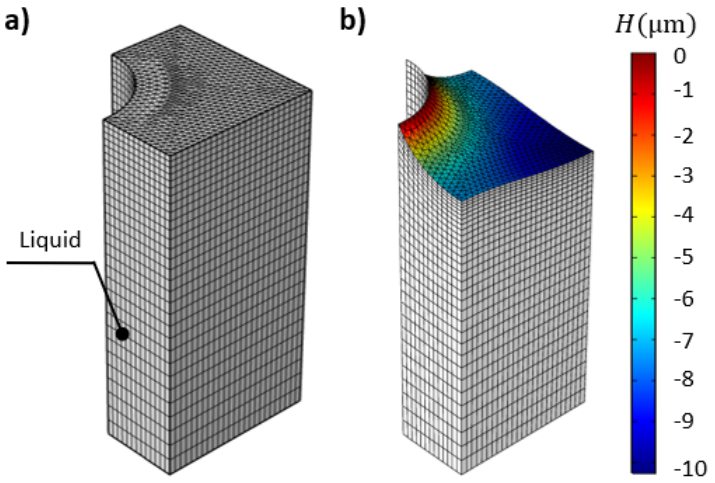

Figure 2.2: **a)** Undeformed quarter unit-cell, and **b)** deformed liquid-vapor interface according to the height expression of the Y-L equation solution in a unit-cell at θ=30° (d=30 μm, l=60 μm, h=60 μm)

In a cell, the balance between the upward surface tension forces on the pillar edge and the downward capillary pressure forces applied on the meniscus result in a static meniscus shape with a solid-liquid contact angle θ. The relation between the capillary pressure and contact angle is obtained by the force balance as follows:

$$p_c(\theta) = \frac{4\sigma\cos(\theta)}{d\left[\frac{4}{\pi}\left(\frac{l}{d}\right)^2 - 1\right]} \tag{2.3}$$

where θ is the contact angle at the three-phase contact line, l is the pitch, and d is the diameter of the pillar.

In order to accurately capture the effect of the interface variation in the wicking direction, a sweep solution for various contact angles is conducted between the flat (θ=90°) and fully stretched menisci (θ=θ_{rec}). The variation of the average and minimum meniscus height according to contact angle are compared in Figure 2.3, and the results show linear-like behavior that makes solving at discrete contact angles and interpolating at the remaining angles possible.

The accuracy of the Y-L equation solutions is ensured by comparing the 3-D meniscus shapes obtained from the simulations with those measured in the study of Adera *et al.* [33] in Sec. 3.1.

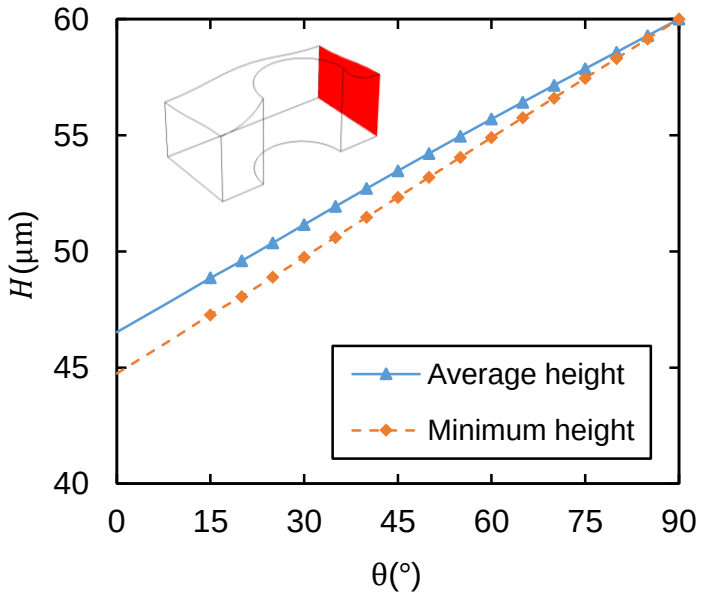

Figure 2.3: Variation of average and minimum meniscus height within a unit-cell (d=30 μm, l=60 μm, h=60 μm) as a function of contact angles. The red plane in the inset indicates the cross-sectional area at which average and minimum meniscus heights are calculated.

2.1.2 Energy Transport

The cell-level thermal model aims to obtain the effective heat transfer coefficient, h_{eff}, as a function of capillary pressure and geometric dimensions. The effective heat transfer coefficient serves as an input for the device-level model, and it is defined in terms of the applied heat flux, q_e'', and the average evaporator superheat, ΔT, as follows:

$$h_{\mathit{eff}} = \frac{q_e''}{\Delta T} \tag{2.4}$$

where the average evaporator superheat is the difference between average evaporator temperature, $T_{e,av}$ (Figure 2.1b) and the vapor temperature, T_v: $\Delta T = T_{e,av} - T_v$. To obtain $T_{e,av}$, temperature distribution at the liquid-substrate interface needs to be found, which is calculated by solving the heat transfer problem at the cell-level.

For the thermal modeling, heat transfer from the pillar top *via* natural convection is negligible (*i.e.* low Nusselt number [12]), and convection in liquid due to the evaporation is negligible (*i.e.* low Péclet number in the vertical direction, Pe $\sim \mathcal{O}(10^{-2})$). Therefore, conduction is the dominant heat transfer mode, and the steady-state conduction equation is solved in liquid and solid for heat transport. Due to the symmetry of the meniscus within a unit-cell, half, quarter or half-of-a-quarter of a unit-cell can be utilized as the computational domain (Figure 2.1b), and thermal symmetry boundary conditions are used on the symmetry surfaces.

A uniform heating ($q = q_e''$) is applied at 5 μm below the liquid-substrate interface to include the constriction resistance of the substrate base [40] Evaporative heat flux is calculated utilizing the kinetic theory of gases. Accordingly, evaporative mass flux can be calculated based on the interfacial properties of the vapor and liquid. At near equilibrium conditions, when the evaporation rate is not excessive, Schrage's original expression [34] reduces to an approximate form [41]:

$$\dot{m}_{evap}'' = \frac{2\hat{\sigma}}{2-\hat{\sigma}} \left(\frac{M}{2\pi R_u}\right)^{1/2} \left(\frac{p_{sat}|_{T_{lv}}}{T_{lv}^{1/2}} - \frac{p_v}{T_v^{1/2}}\right) \tag{2.5}$$

where $\hat{\sigma}$, M, R_u, T_{lv}, $p_{sat}|_{T_{lv}}$, T_v, and p_v are the mass accommodation coefficient,

molar mass of the liquid, universal gas constant, interface temperature, saturation pressure at the interface temperature, vapor temperature, and vapor pressure, respectively. Since conduction across the Knudsen layer is commonly insignificant where non-condensable gases are not present, the assumption of Equation (2.5) is reasonable that considers only heat transfer due to evaporation [47]. Evaporative mass flux is imposed on to the meniscus as the interfacial heat transfer coefficient (h_{int}) to imitate the heat loss from the meniscus *via* evaporation:

$$h_{int} = \dot{m}''_{evap} \left(\frac{h_{fg}}{T_{lv} - T_v} \right) \tag{2.6}$$

where, h_{fg} is the latent heat of vaporization of the liquid. Applying this interfacial heat transfer coefficient together with other aforementioned boundary conditions, the governing equation ($\nabla^2 T = 0$) is solved using the FEM solver of COMSOL Multiphysics software [42].

Mass accommodation coefficient (MAC) is the only unknown parameter in Equation (2.5) which cannot be measured accurately or calculated for polar liquids with molecular dynamics simulations. In the literature, an order of magnitude varying MAC values between 0.02 and 0.6 are used for water [46] since it depends on the experimental setup, working fluid, surface contaminants [46], and temperature. [48]. It is essential to understand the effect of the MAC number on the heat transfer and the evaporator superheat variation since there is no specific MAC value for water. The effect of the mass accommodation coefficient on the evaporator superheat and on the effective heat transfer coefficient is presented as a function of evaporator heat flux in Figures 2.4 and 2.5. As the MAC decreases, evaporation through the meniscus becomes challenging, and notable decreases in h_{eff} occur; the decrease being more pronounced for smaller values that are commonly used in the literature [12, 33, 36].

The thin-film area extends as the contact angle decreases due to the improved curvature; therefore, in Figure 2.4, a substantial enhancement in h_{eff} is observed as contact angles diminish. In order to calculate the thermal resistance at different capillary pressure (or contact angles) in the device-level model, for each pillar configuration, a third-order polynomial consistent with the cell-level model is fitted to h_{eff} as a function of the capillary pressure.

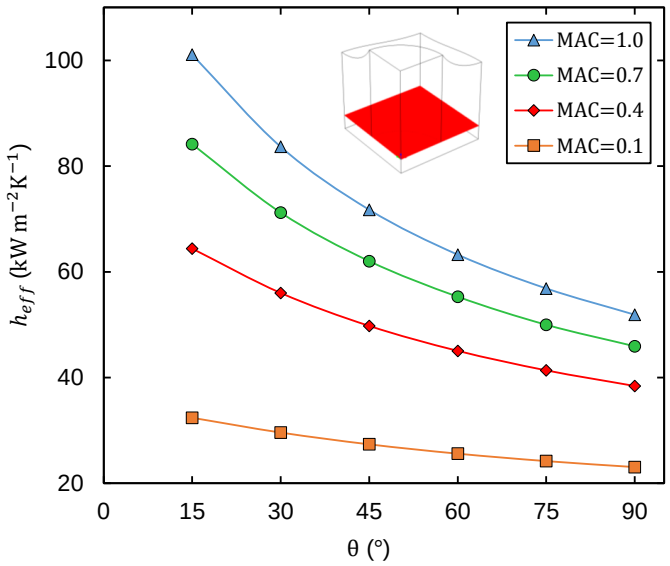

Figure 2.4: Variation of effective heat transfer coefficient within a unit-cell as a function of contact angles for various MAC numbers (d=30 μm, l=60 μm, h=60 μm). The red plane in the inset indicates the cut plane (liquid-substrate contact plane) on which average temperature is calculated to obtain h_{eff} for the wick structure.

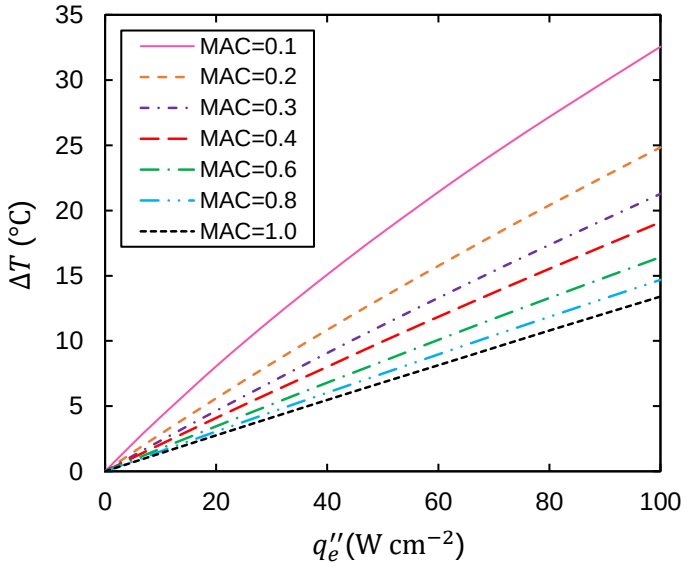

Figure 2.5: ΔT as a function of applied heat flux for various MAC numbers in a unit-cell at θ=30° (d=30 μm, l=60 μm, h=60 μm). A notable increases in superheat temperature is observed as the MAC decreases, and the superheat variation with heat flux becomes non-linear.

2.1.3 Liquid Transport

The cell-level flow model aims to obtain the pillar structure's liquid permeability, κ, in the wicking direction. Permeability serves as an input for the device-level model, and it can be calculated based on Darcy's law. To obtain κ, liquid flow is solved in the half unit-cell domain shown in Figure 2.1c.

In the liquid domain, steady-state Navier-Stokes equations are utilized for the conservation of mass and linear momentum. Due to the dominating surface forces over the body forces ($\mathrm{Bo} = \Delta\rho g l^2/\sigma \sim \mathcal{O}(10^{-4})$), gravity is omitted in the modeling. The flow is laminar ($\mathrm{Re} = \rho u l/\mu \sim \mathcal{O}\left(10^{1}\right)$), and viscous dissipation term is not included in the energy equation because of the low liquid velocities. Evaporative mass flow is neglected since evaporation-induced liquid velocity perpendicular to the meniscus is low ($\mathrm{Re_z} \sim \mathcal{O}\left(10^{-2}\right)$). No shear boundary condition on the meniscus (viscosity of vapor is excessively low to cause friction on the interface), symmetry on the sides, no-slip boundary condition on the solid surface, and periodic boundary condition with a pressure difference between the inlet and outlet of the domain are applied to ensure fully developed liquid flow. With these boundary conditions, Navier-Stokes equations are solved using the finite element method (FEM) solver of COMSOL Multiphysics. Then the resultant flow rate is utilized to back-calculate the permeability, κ, from Darcy's law:

$$\overline{U} = \frac{1}{A_c} \iint u \, dy \, dz = -\frac{\kappa}{\mu} \nabla p \tag{2.7}$$

where $\overline{U}$ is the average velocity, u is the velocity component in the x-direction, A_c is the cross-sectional area at the outlet, μ is dynamic viscosity which is temperature dependent, and ∇p is the pressure gradient.

A sample wick structure is considered for a liquid transport problem with a reference pressure gradient across the cell, and the resultant velocity magnitudes at different cross-sections are illustrated in Figure 2.6. Then the effect of pressure gradient on the average velocity is investigated at different contact angles, and the results are presented in Figure 2.7. Since the variation of $\overline{U}$ linear, the permeability values are obtained by the simulations with a reference pressure gradient.

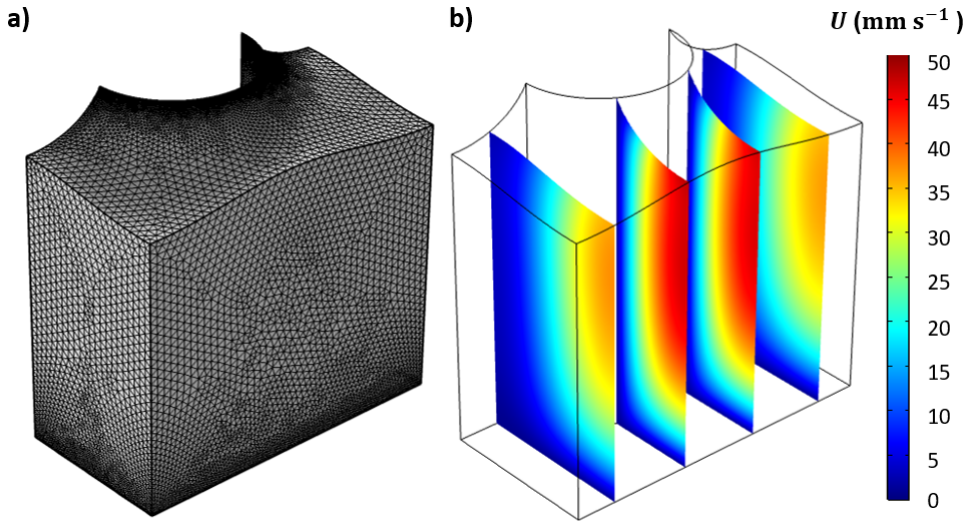

Figure 2.6: **a)** Mesh structure of a sample liquid transport problem for a half unit-cell at θ=30°, and **b)** velocity magnitudes at different cross-sections ($\Delta p_c = 15$ Pa, d=30 μm, l=60 μm, h=60 μm)

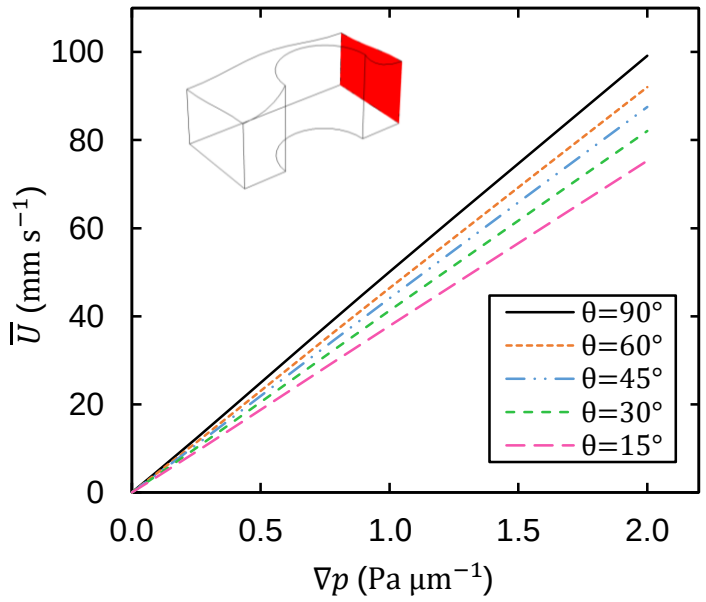

Figure 2.7: The average velocity ($\overline{U}$) of water as a function pressure gradient ($\nabla p = \Delta p_c/l$) at different contact angles are illustrated (d =30 μm, l =60μm, h =30 μm). The red plane in the inset indicates the cross-sectional area (A_c) at which average velocity and permeability of the wick structure at the corresponding contact angle is calculated.

For a set of given pillar array dimensions, the capillary pressure defines the curvature of the interface or the contact angle, and permeability (κ) is a function of local pressure. Solving average velocities for various θ provides the relation between local permeability and capillary pressure. The permeability values at different contact angles (or capillary pressure) are plotted in Figure 2.8 for three wicking structures with different heights. The permeability increases as as the pillar height increases, and the effect of the contact angle on the permeability diminishes. Therefore, the applied pressure gradients for long pillars give similar results at various contact angles. In order to calculate the permeability of the wick structure at different capillary pressures (or contact angles) in the device-level model, a third-order polynomial consistent with the cell-level model is fitted to κ as a function of the capillary pressure.

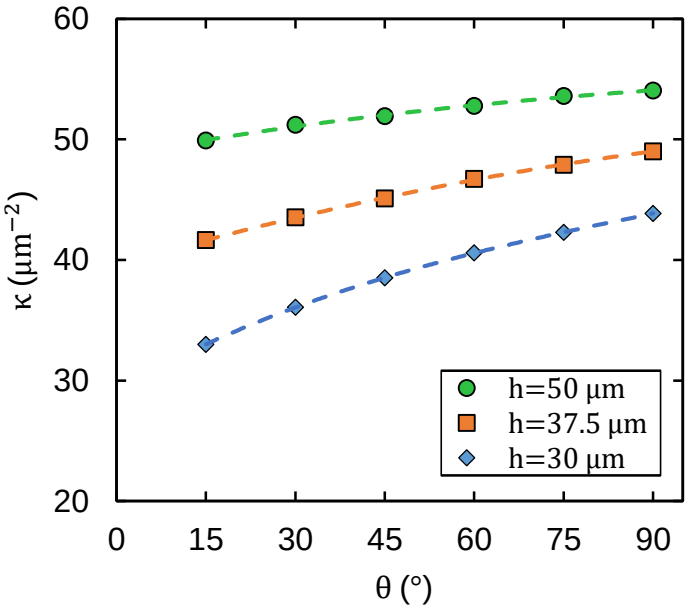

Figure 2.8: Permeability as a function contact angle at different contact angles are illustrated for three different pillar height (d =30 μm, l =60μm). Dashed lines show the third-order polynomial fitted to the permeability values in accordance with the CFD simulations.

2.1.4 Thermocapillary Flow

Thermocapillary flow is driven by the surface tension variation on the liquid-vapor interface originating from the temperature gradients. The impact of thermocapillary flow can be measured with the Marangoni number, which is defined as follows:

$$\mathbf{Ma} = \left(\frac{\partial \sigma}{\partial T}\right)\left(\frac{L_t \Delta T_{int}}{\mu \alpha}\right) \tag{2.8}$$

where L_t is the length scale of the domain (a tangential distance on the meniscus between the pillar edge and a corner of the unit-cell), ΔT_{int} is the maximum temperature difference at the interface, and α is thermal diffusivity of the liquid. Accordingly, in the case of high superheat and/or large pitch, thermocapillary flow can trigger effective internal convection in a cell.

To account for the thermocapillarity driven convective energy transport, full steady state energy equation (with convective terms) is utilized:

$$\rho c_p \mathbf{u} \cdot \nabla T = \nabla \cdot (k \nabla T) \tag{2.9}$$

where ρ is the density, c_p is the specific heat capacity, and k is the thermal conductivity of the liquid. The half unit-cell (Figure 2.1c) is considered as the simulation domain for the multi-physics problem, where cell-level flow and thermal models are coupled in liquid and solid domains. The computational model utilizes temperature-dependent properties throughout the domain, which is specifically crucial to include the effect of viscosity variation. For both flow and thermal problems, symmetry conditions are utilized at the boundaries parallel to the wick (capillary) flow. Inlet and outlet conditions are determined based on periodicity at the boundaries perpendicular to the capillary flow. For the flow, periodic hydrodynamic boundary condition with the pressure difference between adjacent cells ($p_{in} - p_{out} = p_c$) is applied to ensure fully developed liquid flow. For the thermal modeling, application of periodic boundary condition ($T_i = T_{out}$) implies no convective energy transport across cells, yet this approximation is justified because of negligible temperature variation between adjacent cells. At the liquid-vapor interface, the evaporation rate is calculated by using the approximate form of the Schrage's equation [41] as discussed in Section 2.1.2.

The tangential force balance is applied between the thermocapillary and the shear force associated with the liquid at the liquid-vapor interface as follows:

$$-\hat{n} \cdot \bar{\bar{\tau}} \cdot \hat{t} = \nabla\sigma \cdot \hat{t} \tag{2.10}$$

where $\bar{\bar{\tau}}$ is the deviatoric stress tensor defined as $\mu(\partial u_i/\partial x_j + \partial u_j/\partial x_i)$ and $\hat{t}$ is the unit tangential vector. With these boundary conditions, governing equations are simultaneously solved using the FEM solver of COMSOL Multiphysics. Thereafter, permeability (κ) and heat transfer coefficients (h_{eff}) at various heat fluxes are stored to create lookup tables for a given geometry. Parametric simulations are performed at different contact angles and heat fluxes for a wide range of pillar array dimensions to observe the impact of the thermocapillary flow in the device-level model.

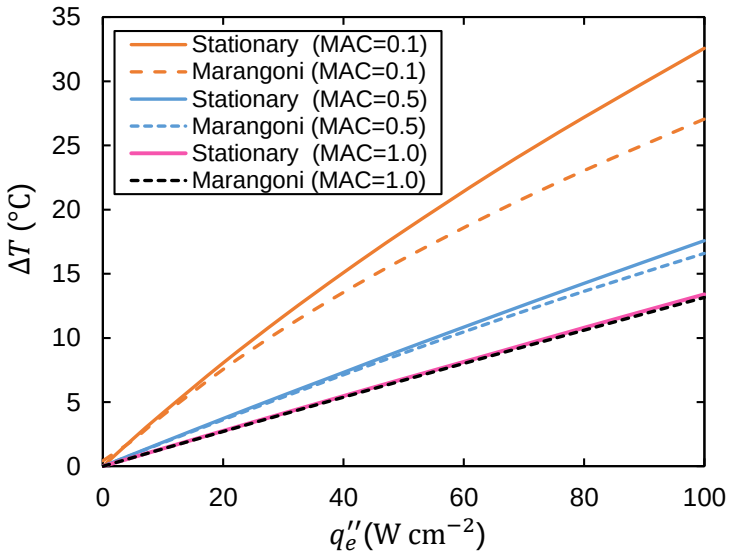

Figure 2.9: Comparison of evaporator superheat (ΔT) predictions by the thermocapillary model and the model discussed in Sec. 2.1.2. Evaporator superheat values (ΔT) are plotted as a function of the applied heat flux for a half unit-cell at θ=30° (d=30 μm, l=60 μm, h=60 μm).

In Figure 2.9, the evaporator superheat (ΔT) predictions by the thermocapillary flow at different MAC values are compared with the superheat predictions by the model discussed in Sec. 2.1.2. The superheat predictions of the two models drift apart as the MAC number decreases and the applied heat flux increases since thermocapillary flow-inducing surface stresses are functions of the thermal gradient.

2.2 Device-level Model

The device-level model is formulated by combining the energy and liquid transport in the discretized domain with the finite element method. In the device-level model, the energy transfer via phase change is modeled by the product of the mass flow rate and the latent heat of evaporation. Mass loss due to the evaporation is compensated by replenishing flow, which is driven by the variance of the capillary pressure along the wicking direction. The liquid replenishing is maintained until the contact angle of the meniscus in a unit-cell reaches the receding contact angle, which is herein denominated as the receding onset, and the corresponding heat flux is called dryout heat flux for a given set of pillar array dimensions.

In the model, a heat input, $q''_{in}(x)$, is applied at the bottom surface of the substrate with a base thickness of t_s (Figure 2.10). The contact angle at the inlet is assumed as 90° (p_c=0) since the wicking structure is observed to be in contact with fluid in the experiments, and flow is inhibited at the outlet due to the termination of the wicking structure. Only evaporative heat transfer is accounted for the energy transfer mechanism from the heated micropillar substrate to the ambient. The device-level model is established based on the flow (see Figure 2.10a) and conduction (see Figure 2.10b) domains, which are discretized in accordance with the unit-cells utilized in the cell-level modeling. Then all cells are linked to satisfy the conservation of mass, momentum, and energy by an outer iterative loop to imitate the thin-film evaporation from a regularly packed pillar array evaporator.

Initially, the conduction in the substrate is ignored (i.e., $q''_{in}(x) = q''_e(x)$), and the device-level flow model is solved to obtain p_c distribution along the wicking direction by assessing the conservation of mass, momentum and energy. The capillary pressure and mass flux at the inlet are sufficient to acquire capillary pressure distribution over the entire domain since the pressure drop depends on permeability (κ) and mass flow rate ($\rho A_c \overline{U}$) according to Darcy's law. Since the applied heat flux is removed solely by the evaporation, the corresponding total liquid mass flux is calculated as the inlet boundary condition, and the capillary pressure-dependent permeability values for each cell are obtained from the look-up tables generated *a priori*.

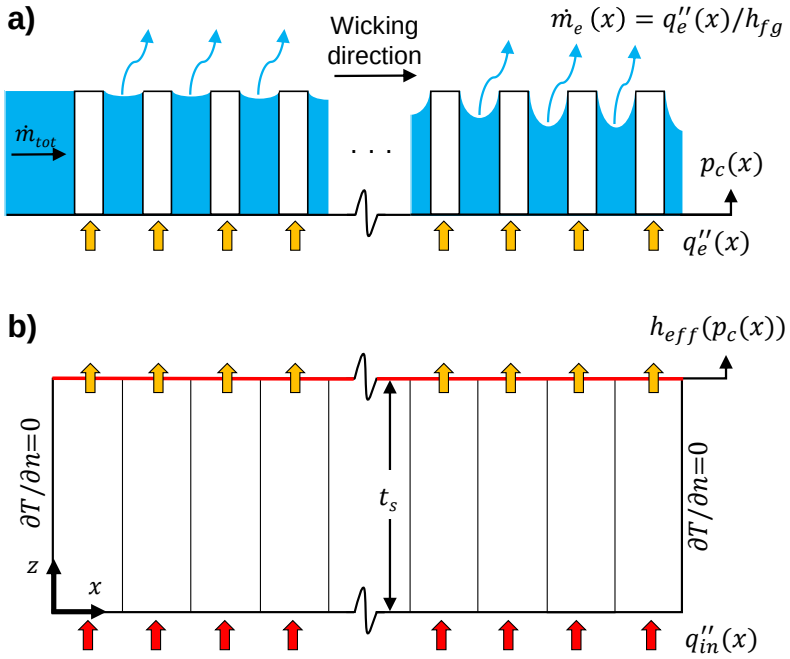

Figure 2.10: Representation of the device-level model for thin-film evaporation. **a)** In the device-level flow model; pressure distribution along the wicking direction is calculated by Darcy's law. Each unit-cell has a unique meniscus with different curvature and capillary pressure thereof. **b)** In the device-level conduction model; capillary pressure-dependent effective heat transfer coefficient is assigned at the top surface of the substrate base, and arbitrary heat flux is applied at the bottom of each unit-cell. Heat transfer through the side walls is assumed negligible.

Since h_{eff} is a function of capillary pressure, once having p_c variation along the wicking direction in the fluid domain, the spatial distribution of $h_{eff}((p_c(x)))$ is utilized in the device-level conduction domain (Figure 2.10b). Due to the presence of axial conduction through the substrate, a non-uniform effective heat transfer coefficient (h_{eff}), and non-uniform evaporation thereof, occurs along the wicking direction. Consequently, the evaporative heat flux $q_e''(x)$ at each cell and average fluid temperature (T_f) is obtained in the conduction domain. Then $q_e''(x)$ and T_f are utilized in the fluid domain to acquire p_c distribution in the second and subsequent iterations. Thermal and flow domains are solved iteratively until the dryout heat flux, and evaporator superheat convergence.

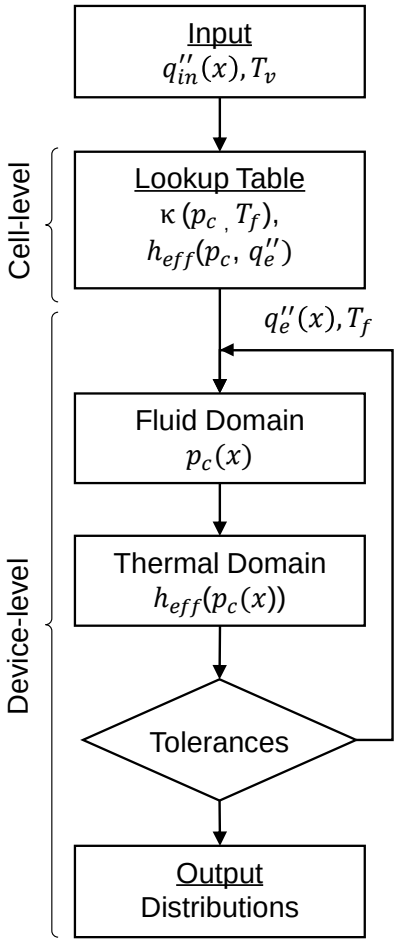

Figure 2.11: Computational scheme. In the beginning, look-up tables are generated at various heat fluxes. In the first iteration, $p_c(x)$ is calculated by neglecting the axial conduction in the substrate. However, the applied heat flux at the bottom of the substrate results in non-uniform evaporation through the axial conduction due to the spatial variation of h_{eff}. In the subsequent iterations, $q''_e(x)$ and T_f are utilized in the fluid domain to acquire p_c distribution, and capillary pressure distribution is utilized in the thermal domain to calculate the temperature distribution in the substrate. Conduction and flow domains are solved iteratively by an outer loop until convergence.

CHAPTER 3

VALIDATION OF MODELS

The current model is validated against three distinct sets of experiments conducted in previous studies [11, 33, 35], where all substrates were made of silicon with a wide variety of pillar dimensions, and the working liquid was deionized water. Varying heat inputs were applied under different ambient conditions. The current model's abilities to predict dryout heat flux, evaporator superheat, and the effect of thermocapillarity is investigated. Since the validation of the heat transfer coefficient can be easily achieved by adjusting the mass accommodation coefficient in Schrage's equation, the concurrent validation of the dryout heat flux and heat transfer coefficient is crucial for Marangoni flow. The substrates with similar pillar dimensions led to the near predictions for the dryout heat flux or superheat values. Accordingly, selected cases from these studies (see Table 3.1) are included in the validation of the model for brevity. Pillar dimensions were sufficiently small for all experiments to prevent the incipience of boiling.

Table 3.1: Details of the micropillar wick evaporators and experimental conditions in previous experiments [11, 33, 35], which are simulated by the proposed model.

	Dimensions (μm)						
Device ID	d	l	h	θ (°)	T_{sat}(°C)	q''_{in}(W cm^{-2})	Ma
Device-A1 [11]	7	20	20	90 →15	100*	0–47	-
Device-A3 [11]	6	50	19	90 →15	100*	0–27	-
Device-1 [33]	5	12	82	90 →70	24	0–46	36–30
Device-5 [33]	12	20	90	90 →70	24	0–45	74–62
Sample-1 [35]	23.4	41.0	39.5	90 →10	25	0–28	73–40
Sample-2 [35]	25.9	41.0	39.5	90 →10	25	0–22	49–32
Sample-3 [35]	28.2	41.0	39.5	90 →10	25	0–23	36–23
Sample-4 [35]	22.1	41.0	39.5	90 →10	25	0–23	77–51
Sample-5 [35]	23.4	36.0	39.5	90 →10	25	0–22	32–20
Sample-6 [35]	23.4	34.0	39.5	90 →10	25	0–20	22–14
Sample-7 [35]	23.4	44.0	39.5	90 →10	25	0–25	97–64
Sample-8 [35]	23.2	41.0	79.7	90 →10	25	0–60	293–215

* Evaporation into the air environment at 1 atm.

3.1 Meniscus Shape

In the Meniscus Shape model, height expression is obtained for the liquid-vapor interface by solving the Young-Laplace equation (assuming a fully-pinned three-phase contact line to the pillar top) for a pillar configuration and contact angle. The height expressions are utilized to form the three-dimensional deformed meniscus as a problem domain for remaining cell-level models. Although a sweep solution for various contact angles is conducted to capture the effect of the interface variation in the wicking direction, the accuracy of the entire model is very sensitive to the interface shape, especially near the pillar edge (contact line), where evaporation intensifies due to thinning film. The meniscus shape model is validated based on the laser interferometry measurements conducted by Adera *et al.* [33]. In the experiments, the vertical deformation in the lateral and diagonal directions was measured between adjacent cell centers, and several data were obtained along both directions.

In Figure 3.1, height expressions obtained by solving the Y-L equation at several contact angles are compared with the experimentally measured vertical deformation data ($d = 5\,\mu\mathrm{m}$, $l = 12\,\mu\mathrm{m}$, $h = 82\,\mu\mathrm{m}$). As shown in Fig.3.1a, in the diagonal direction, vertical deformation prediction of the simulation for the pillar (receding) contact angle of θ=74° matches best with the experiment, whereas in the lateral direction, vertical deformation prediction of the simulation for the pillar (receding) contact angle of θ=66° matches best with the experiment. The average pillar contact angle can be calculated as 70° considering the results in both directions. This value exactly matches with the average pillar contact angle prediction of Adera *et al.* [33].

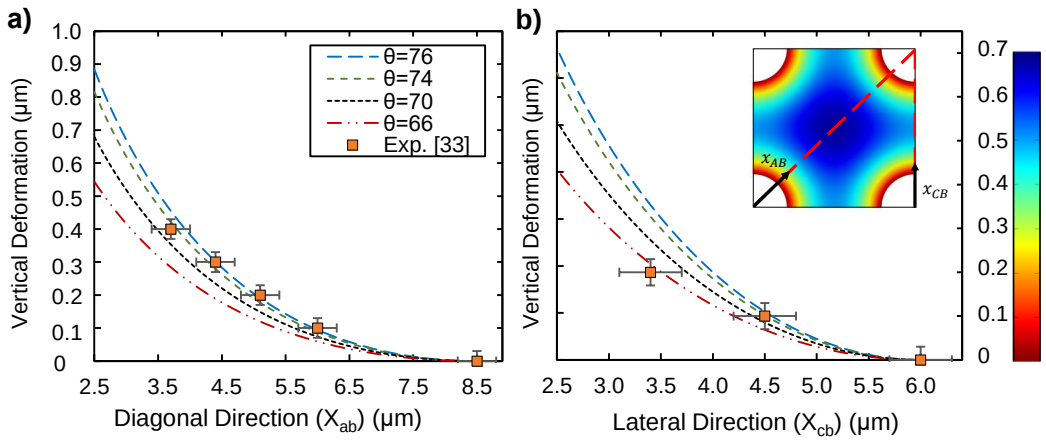

Figure 3.1: Comparison of vertical deformation prediction of the simulation and the experimental laser interferometry measurements [33]. Vertical deformation along the **a)** diagonal and **b)** lateral directions. The inset in Figure 3.1b demonstrates vertical deformation contours on a meniscus with the contact angle of 70°.

3.2 Dryout Heat Flux

In the first experimental work [11], simulated by the proposed model, evaporation took place into the air from two different samples (Device-A1 and Device-A3 in Table 3.1). Schrage's equation is valid in a vacuum environment, and the effect of the partial pressure of the fluid must be considered to predict the rate of evaporation in the ambient condition. While the pillar diameter and height were close, the pitch of the pillars was different ($50\,\mu\mathrm{m}$ vs. $20\,\mu\mathrm{m}$) in these substrates. Accordingly, the permeability of the substrates differs substantially. In the experiments, as expected, a substrate with high permeability maintained the liquid feeding to a longer distance for the same heat input, whereas the substrate a with denser pillar forest could withstand a higher heat load without drying for the same liquid wicking length. The predictions of the proposed model excellently match with the experimental measurements as shown in Figure 3.2, where maximum wicking lengths at the onset of dryout are presented for different heat fluxes. While this comparison reflects the success of the proposed model in terms of liquid transport, the model's sensitivity to the thermal effects could not be assessed since temperature measurements were not made during the experiments.

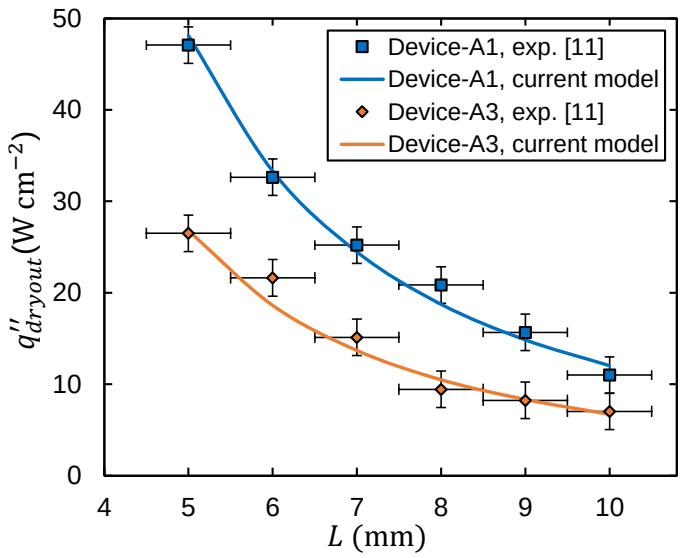

Figure 3.2: Comparison of the dryout heat flux predictions of the proposed model and the experimental results of Zhu *et al.* [11].

3.3 Evaporator Superheat

Secondly, the experimental work of Adera *et al.* [33] is utilized to verify the thermal capabilities of the proposed model. In their experiments, the evaporation took place into a controlled environment with pure vapor, and the wicks were in contact with the liquid at the four sides of the substrate. Accordingly, bi-directional liquid flow is considered in the current model to represent the physics accurately (see Appendix A.2 for the details of bi-directional flow modeling). A relatively high receding contact angle (θ_{rec} =70°) was observed in the experiments, which was attributed to the presence of polymer remaining on the pillars. The substrate temperature was measured at different heat fluxes by gradually increasing the applied heat input, and the average temperature at the evaporator was estimated through a one-dimensional thermal resistance model. These average evaporator temperature estimations of Adera *et al.* [33] are successfully predicted by the proposed model as shown in Figure 3.3, where the average temperature is represented by the average evaporator superheat.

It should be noted that evaporator temperature is primarily dictated by the rate of evaporation, which determines the limitations of the evaporative cooling. Therefore, calculation of the evaporation rate *via* Schrage's approximate expression (Equa-

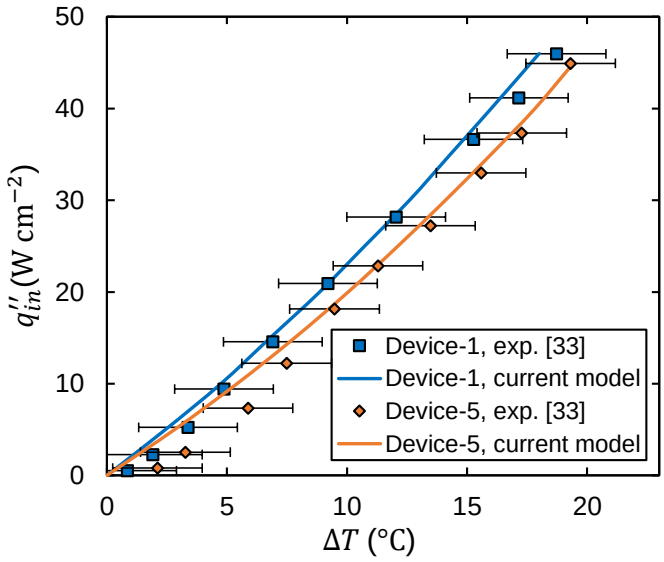

Figure 3.3: Comparison of the average evaporator superheat predictions of the proposed model and the experimental results of Adera *et al.* [33]. For both devices, MAC value of 0.06 is used in the estimation of evaporation rates.

tion (2.5)) has a substantial effect on the predicted temperatures in the current model. However, Schrage's expression includes a parameter, $\hat{\sigma}$, the mass accommodation coefficient, which does not possess a common universal value. In fact, it is a system-dependent parameter [36], which varies with the type of the liquid, system cleanliness, etc.. From the kinetic theory point of view, a departure from the equilibrium alters the macroscopic vapor (drift) velocity and the thermophysical properties in the vapor. These effects influence the value of MAC utilized in the estimation of evaporation since evaporation is inherently a shifting equilibrium phenomenon. Further discussion is out of the scope of this study, and past studies focusing on MAC [43], or evaporation/condensation coefficients [44] offer a broader perspective. The proposed strategy in the current work was to determine a MAC value for each device and utilize this value for the experiments conducted on the same device. A system-specific MAC is obtained with this approach, which enables accounting for the uncontrollable parameters associated with the experimentation. Assigning different MAC values to each experiment is not practical when modeling is performed for design purposes, and it might break the connection between MAC and the system by turning MAC into a fudge factor serving as a fitting parameter between each simulation and experiment.

3.4 Thermocapillary Flow

The presence of polymer remaining on the pillars fabricated for the study of Adera *et al.* [33] makes those experiments inappropriate for the investigation of the effect of thermocapillary flow on the evaporation from micropillar evaporators since the presence of a small amount of contamination on the water interface is known to hinder the induction of a Marangoni flow [45]. On the other hand, the study of Wei *et al.* [35] provides a suitable base for the investigation of thermocapillary flow by providing a set of evaporation experiments into pure vapor environment across a wide range of Ma numbers (see Table 3.1). Moreover, the observation of the low receding contact angle of water ($\theta_{rec} = 10°$) suggests contamination-free pillars. Therefore, the current model is applied to simulate the experiments of Wei *et al.* [35].

Three different scenarios are modeled to assess the individual effects of temperature variation and Marangoni flow: i) isothermal model, ii) non-isothermal model, and iii) Marangoni model. In the isothermal model, the liquid temperature is set to the vapor temperature, and the liquid temperature increase associated with the applied heat load is neglected. This simplification directly affects the thermophysical properties, especially the liquid viscosity, which is appreciably sensitive to the temperature. In the non-isothermal model, on the other hand, the liquid temperature increase is obtained from the cell-level thermal model, and the modeling is performed using temperature-dependent thermophysical properties. In the Marangoni model, thermocapillary convection is also included such that all active transport mechanisms are taken into consideration in the model.

The first comparison is made for the dryout heat fluxes as shown in Figure 3.4a. Since the temperature rise is relatively restricted for the first seven samples, predictions of isothermal and non-isothermal models are close. However, for Sample-8, which has the highest heat input, the isothermal model fails to correctly predict the dryout heat flux due to the omission of thermal effects. A similar trend is also observed for the Marangoni model. Moderate variation of interfacial temperature keeps Ma number relatively small (see Table 3.1), which leads to almost identical results for non-isothermal and Marangoni models in the first seven samples. Yet, for Sample-8, there is a small deviation between the dryout heat flux predictions of non-isothermal

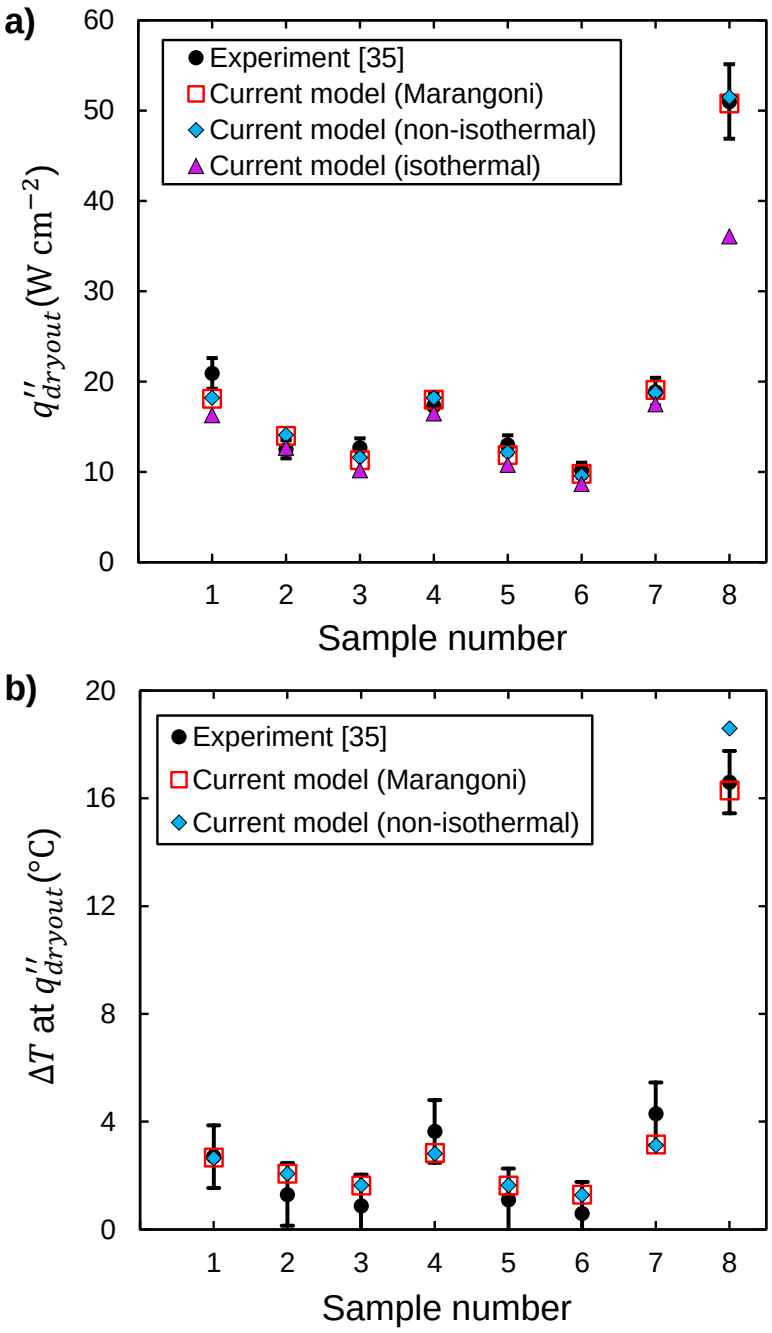

Figure 3.4: Comparison of the **a)** dryout heat flux and **b)** average evaporator superheat predictions of the proposed model and the experimental results of Wei *et al.* [35]. Different MAC values between 0.1 and 0.4 are assigned to each sample and the assigned value is utilized for all experiments conducted on the corresponding sample in the estimation of evaporation rates.

and Marangoni models. Moreover, the predictions of the Marangoni model is closer to the experimental results, which gives a clue for the effect of thermocapillary convection. However, this small difference prevents making a solid conclusion. Then the second comparison is made, now, for the average evaporator superheats as shown in Figure 3.4b. At this time, the isolated effect of thermocapillary convection is apparent. For Sample-8, the non-isothermal model fails to predict the average evaporator superheat, whereas the Marangoni model successfully predicts it.

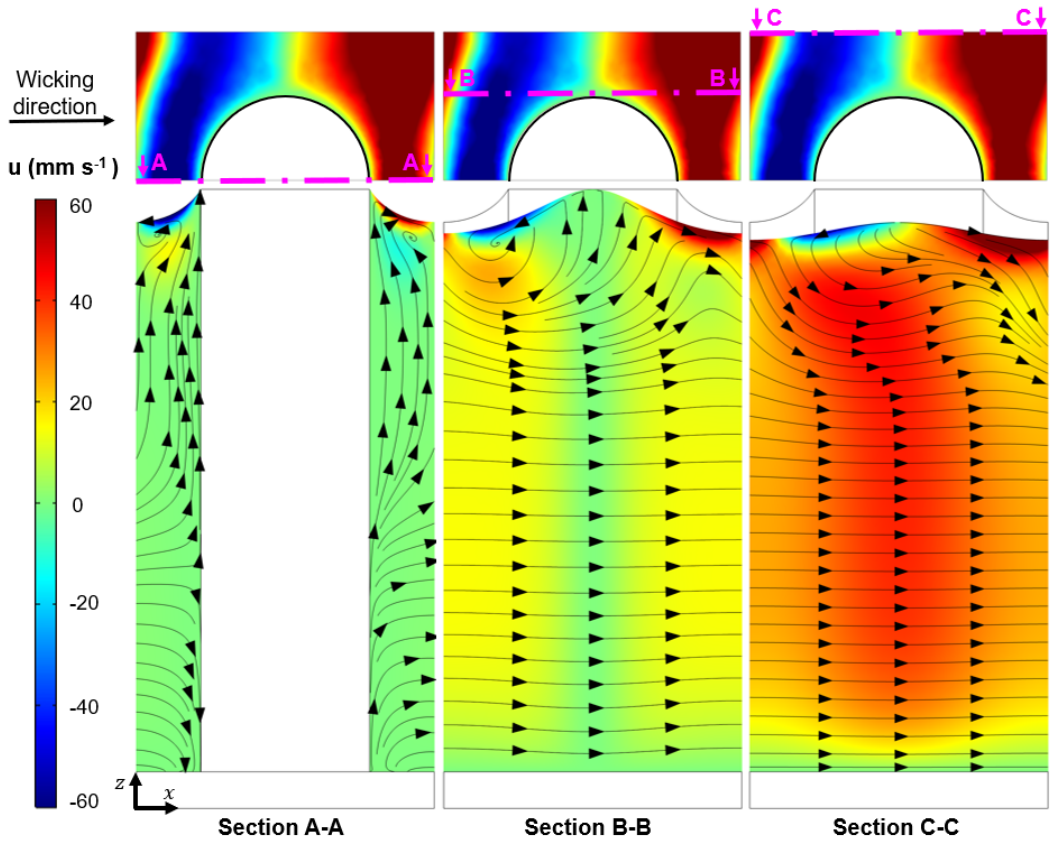

Figure 3.5: Magnitude of the velocity component in the wicking direction with superimposed streamlines at different cross-sections of a unit-cell parallel to the wicking direction. Positions of cross-sections are (as specified in the top view): **a)** at the pillar center, **b)** at the pillar edge, and **c)** at the symmetry center between adjacent unit-cells. Results are given for Sample-8 experimented in Ref. [35] at a heat load of $q''_e = 50\,\mathrm{W\,cm^{-2}}$ for a unit-cell with the contact angle of $\theta = 30°$.

Since the average temperature of Sample-8 is substantially affected by the thermocapillarity, Marangoni convection is expected to have a dominant effect on the the liquid flow near the liquid-vapor interface. To reveal this, liquid flow patterns at different cross-sections of a unit-cell parallel to the wicking direction are presented in Figure 3.5 for Sample-8. As shown in all cross-sections, thermocapillarity induces surface flows leading to circulation to a varying extent. While these surface flows are in the same direction with the wicking (capillary) flow at the downstream-half of a unit-cell, they oppose the wicking flow at the upstream-half of a unit-cell. The origin of these thermocapillary surface flows is the interfacial temperature variation. Resultant temperature distributions on the interface (top view) together with different views parallel to the wicking direction are provided in Figure 3.6. As shown in the top view, a thermal boundary layer with a significant temperature gradient develops on the liquid-vapor interface near the pillar contact line. This temperature gradient triggers a radially outward surface flow from the warmer pillar contact line to the cooler zones around the pillar, leading to the flow patterns shown in Figure 3.5. In addition, the temperature field and superimposed velocity streamlines at the cross-section near the pillar edge in two adjacent unit-cells are demonstrated in Figure 3.7

The formation of periodic reverse surface flows is expected to decrease the mass transport in the wicking direction. Accordingly, the dryout heat flux is expected to decrease due to the associated capillary flow deficit. The extent of the deficit, on the other hand, scales down with the pillar height since the permeability of a wick with substantially long pillars is slightly affected by the dynamics of the surface flows. The capillary flow through the pillars of Sample-8, for instance, exhibits an undisturbed parallel flow pattern in the wicking direction except for a restricted near interface zone affected by the thermocapillarity, which penetrates through the liquid film no more than a quarter of the pillar height (see Figure 3.5b-c). Therefore, dryout heat flux is slightly affected by the presence of Marangoni flow in Sample-8. On the other hand, thermocapillary flow significantly enhances convective energy transport. As it can be seen in Figure 3.6, energy transport paths follow the velocity streamlines by manifesting the convection as the primary energy transport mechanism. The warmer liquid is moved away from the pillar contact line with the surface flow so that cooler fresh liquid from the outer region replenishes it.

The resultant circulation creates an effective mixing mechanism, which enhances the evaporation and the associated interfacial heat transfer coefficient. Accordingly, average evaporator temperature significantly drops (*ca.* 3 °C) in the presence of Marangoni convection compared to the evaporation with the stationary liquid assumption.

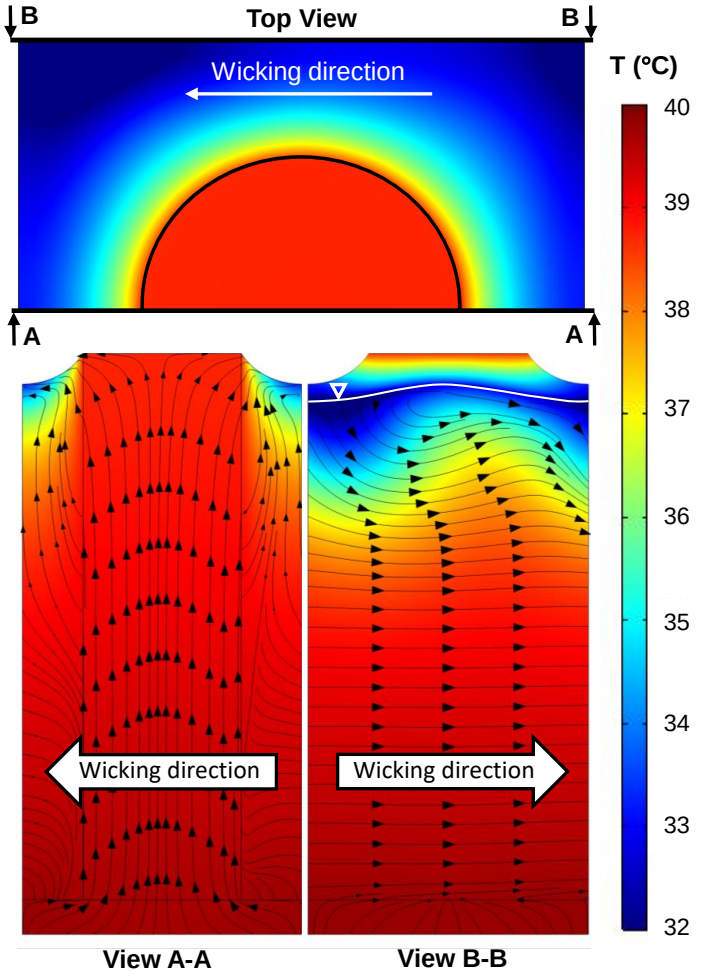

Figure 3.6: Temperature field and superimposed total energy flux streamlines on the interface (top view), pillar center plane (view A-A), and symmetry center plane between adjacent unit-cells (view B-B). In view B-B, the liquid-vapor interface is shown by white solid line. Results are given for the Sample-8 experimented in Ref. [35] at a heat load of $q''_e = 50\,\mathrm{W\,cm^{-2}}$ for a unit-cell with the contact angle of $\theta = 30°$.

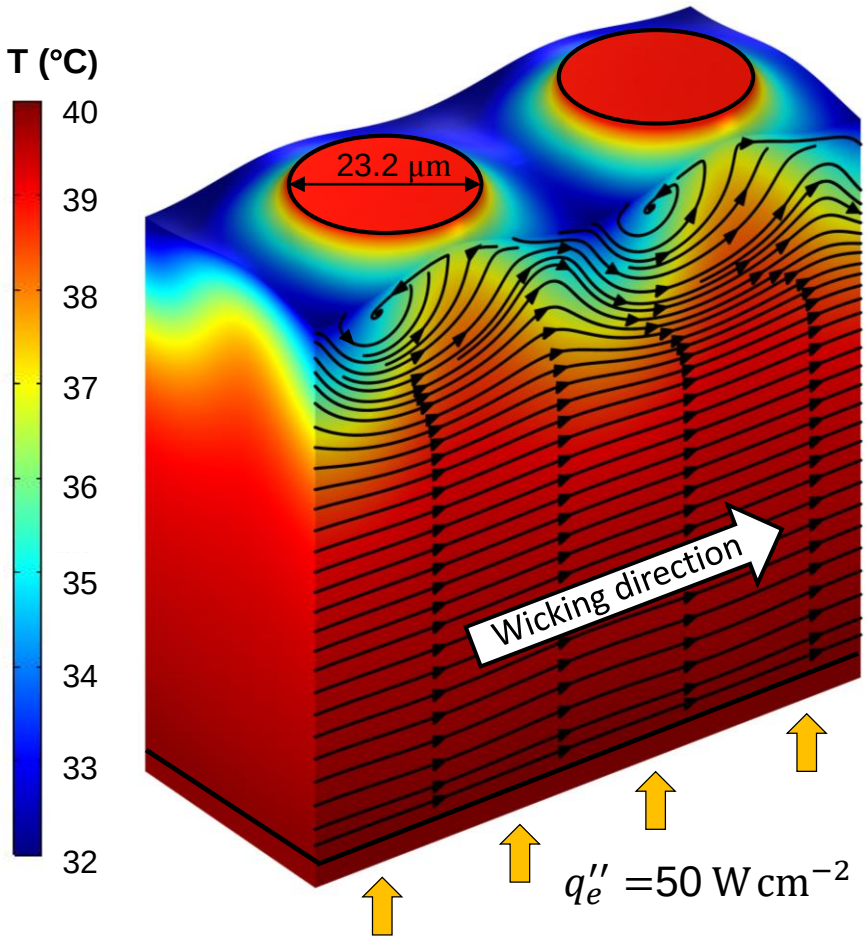

Figure 3.7: Temperature field and superimposed streamlines at a cross-section near the pillar edge for Sample-8 at a heat load of $q_e'' = 50\,\mathrm{W\,cm^{-2}}$ for a unit-cell with the contact angle of $\theta = 30°$.

CHAPTER 4

DESIGN STUDIES

There are two characteristics that determine the performance of a micropillar thin-film evaporator, as aforementioned; dryout heat flux that limits the passive replenishing flow and the effective heat transfer coefficient (or effective thermal resistance). The wick structure can be optimized by maximizing the heat transfer coefficient (minimizing the evaporator superheat) and sustaining the dryout heat flux at a reasonable level. In addition, it is necessary to consider the evaporator superheat temperature to avoid instability such as nucleation boiling due to excessive temperature on the liquid; however, nucleation boiling is out of the scope of this study.

In this chapter, an optimization study for hypothetical but realistic thermal requirements (q''_{in} =50 $\mathrm{Wcm^{-2}}$, ΔT < 12 °C, L =10 mm, θ_{rec} =15°) is conducted to guide engineers for micropillar evaporator design. Initially, the effect of the pillar ratios (l/d, d/h) on the dryout heat flux and effective heat transfer coefficient are investigated by keeping diameter constant (d=30 μm). Second, the effect of diameter on q''_{dryout} and ΔT is examined over a wide range by maintaining the pillar ratios constant at the chosen values. In this procedure, pillar diameter and pillar ratios (d/h, l/d) can be specified to satisfy the predetermined thermal requirements. Then a final sweep solution is conducted in this limited region to find optimum pillar dimensions with a minimum thermal resistance (lowest evaporator temperature) and sufficient dryout heat flux within the desired tolerances. Finally, the effect of thermocapillarity is investigated on the optimized wick structures. The highest MAC value employed validating the experiments, 0.4, is utilized in this chapter.

4.1 Effect of porosity and aspect ratio

Numerous optimization studies in the literature addressed porosity and aspect ratio to maximize dryout heat flux and/or thin film evaporation. Zhu *et al.* [11] focused to maximize q''_{dryout} with optimal aspect ratio (d/h) between $0.4 - 0.6$, and a pitch-to-diameter ratio ~ 3.0. On the other hand, Farokhnia *et al.* suggested an optimum pitch-to-diameter ratio, $l/d \sim 1.8$, to maximize the heat flux by thin-film evaporation [30]. However, later studies addressed the simultaneous optimization of h_{eff} and q''_{dryout} by emphasizing the requirement of the optimization study in accordance with the maximum thermal load, allowed superheat and microfabrication constraints [12, 36].

The effect of porosity and aspect ratio are investigated in Figure 4.1 to understand the impact of pillar dimensions on the dryout heat flux at the device level and effective heat transfer coefficient at the cell-level. Although permeability increases with l/d, lack of capillary pressure due to the separated wick structures adversely affects wicking performance and decreases q''_{dryout}. Therefore, there is an optimal l/d ratio between 2-4 depending on the aspect ratio (d/h) that maximize q_{dryout}. While increasing the pillar height significantly enhances dryout heat flux, it remarkably reduces h_{eff} as seen in Figure 4.1b. The aspect ratio between $0.4 - 0.6$ promises better thermal and wick performance for relatively low pitch-to-diameter ratios since the difference between h_{eff} becomes less pronounced as l/d ratio is reduced.

Secondly, the effect of the pillar diameter for a fixed aspect ratio d/h=0.5 and three different pitch-to-diameter ratios (l/d=1.6, 2.0, 3.0) is investigated in Figure 4.2. Increasing pillar diameter (with increasing pillar height) significantly increases the dryout heat flux for all pitch-to-diameter ratios. There is a slight temperature variation for l/d between 1.6 and 2.0; on the other hand, a notable increase in the dryout heat flux is observed. Considering both performance metrics of a micropillar evaporator, l/d between $1.6 - 2.0$ and d/h between $0.4 - 0.6$ should be chosen. The pillar diameter should be determined depending on the desired dryout heat flux and superheat temperature limitations.

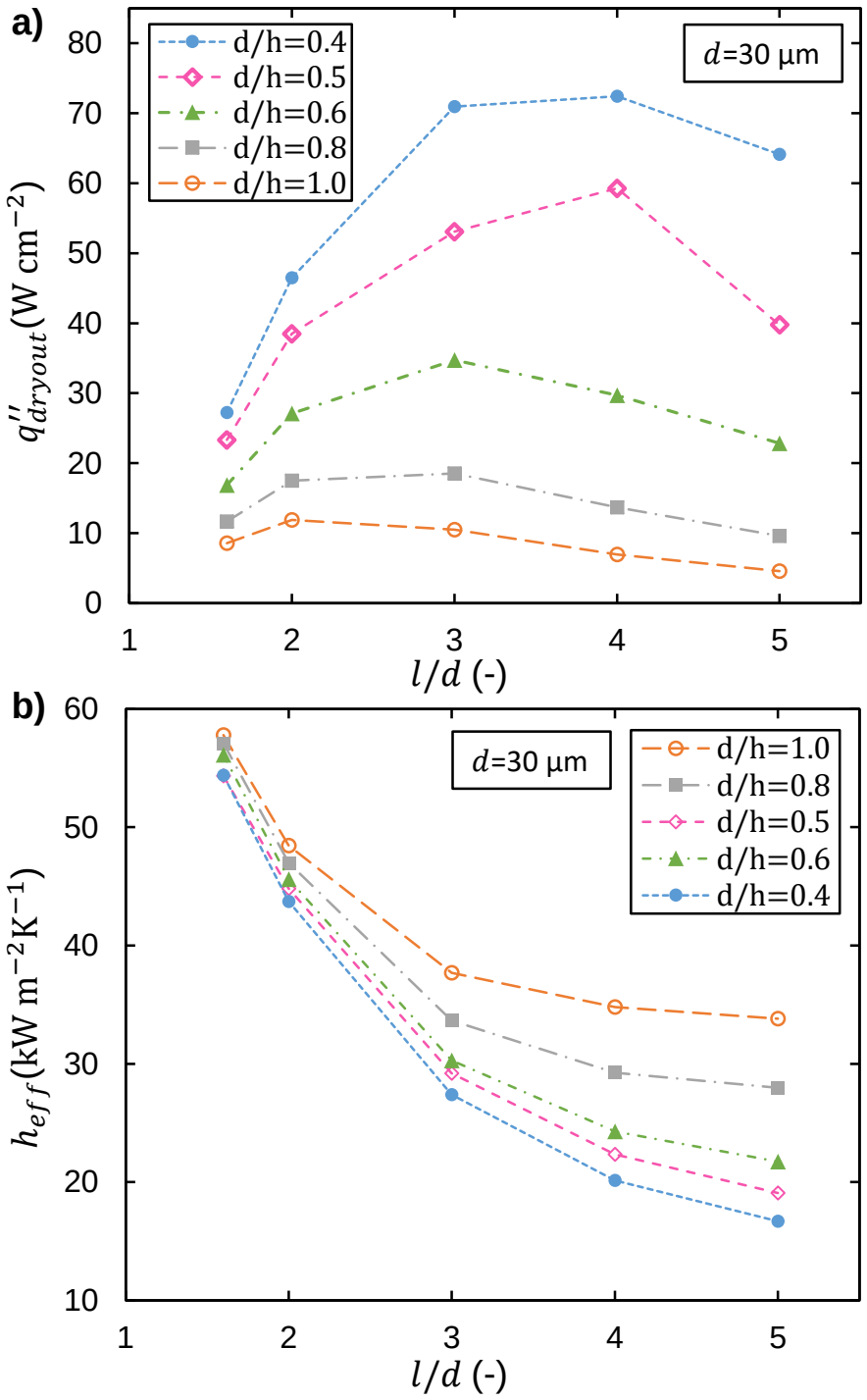

Figure 4.1: The effect of pitch-to-diameter ratio and aspect ratio on **a)** dryout heat flux (L=10 mm), **b)** cell-level h_{eff} at θ=45°, d=30 μm.

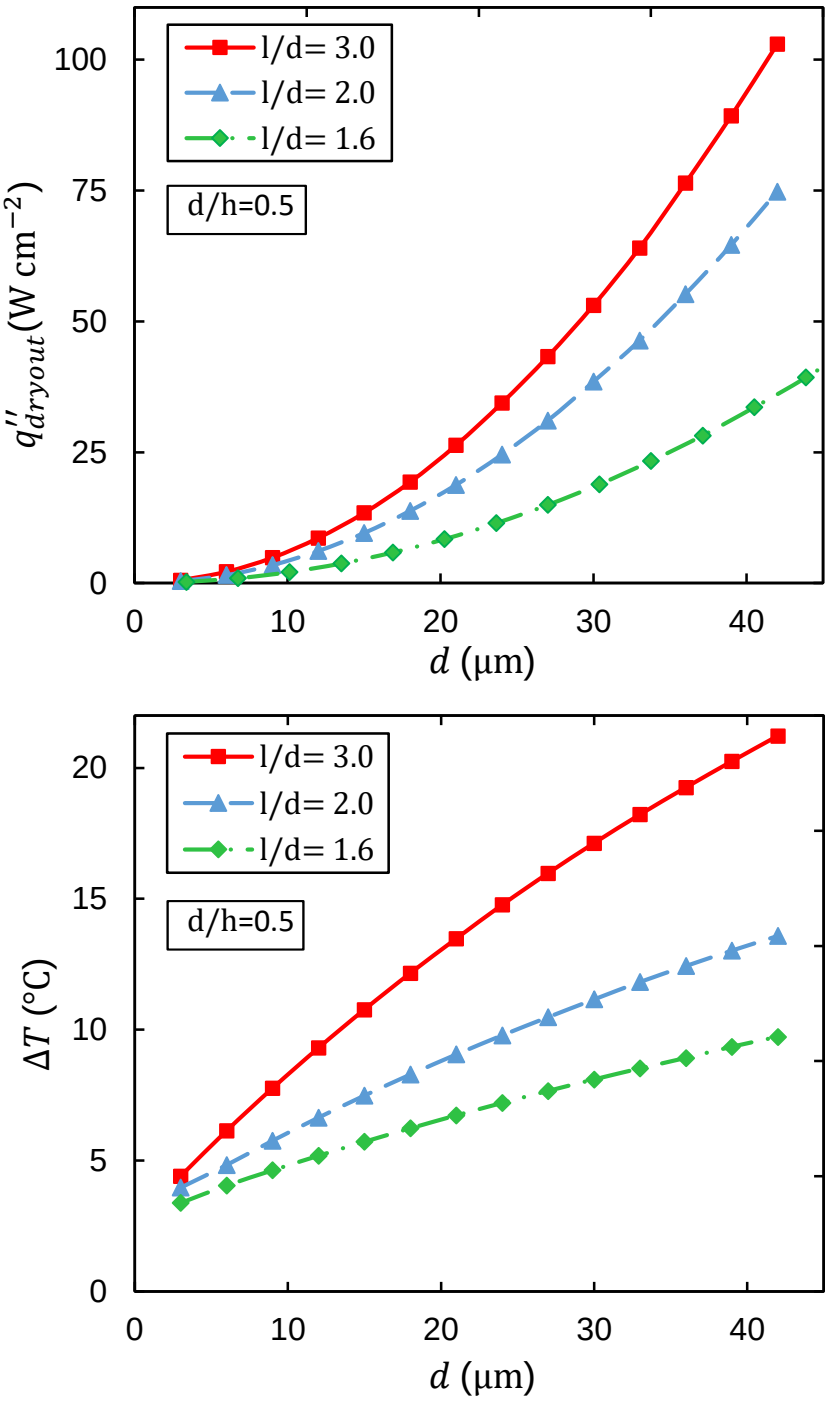

Figure 4.2: The effect of diameter with three pitch-to-diameter ratio for **a)** q''_{dryout} (L=10 mm), **b)** ΔT values in a unit-cell at θ=45° for q''_e=50 W cm^{-2} heat load (d/h=0.5).

4.2 Optimization study

According to Figure 4.2, the pillar diameter should be around 40 μm to obtain adequate performance for the electronic component with 50 W cm^{-2} uniform heat load, and the aspect ratio and pitch-to-diameter ratio should be investigated for optimum pillar dimensions. Therefore, the final iteration to obtain such an optimized pillar configuration is conducted for three different diameters (d= 35, 40, 45 μm), three different pitch-to-diameter ratios (l/d= 1.6, 1.8, 2.0) and three different aspect ratios (d/h=0.4, 0.5, 0.6) to assess the performance of various wick structures on the dryout heat flux and average evaporator temperature with the substrate thickness of t_s= 650 μm, total wicking length L=10 mm, and applied heat flux of q''_{in}= 50 W cm^{-2}.

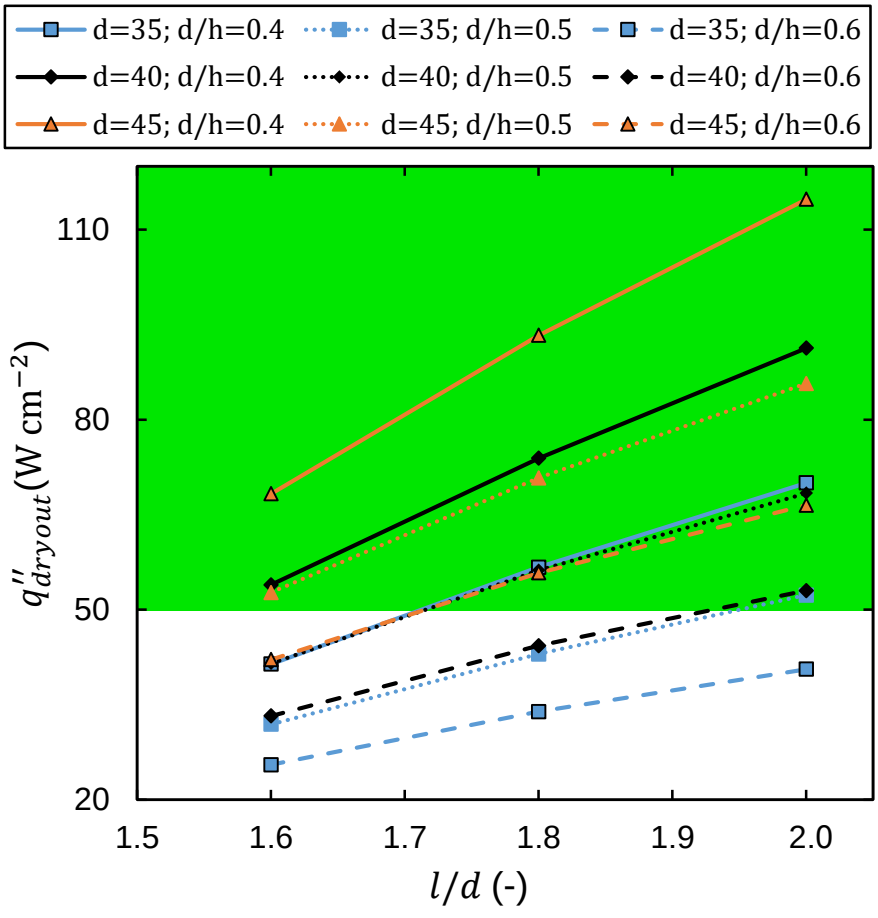

Figure 4.3: Dryout heat fluxes of various pillar structures in near-optimum region. The green rectangle indicates the required heat flux for the design (t_s=650 μm, L=10 mm, q''_{in}=50 W cm^{-2})

Dryout heat fluxes of the devices under uniform heat load for 10 mm wicking length are presented in Figure 4.3, and green rectangle indicates the allowable dryout heat fluxes for the design. As expected, broader and taller pillars can dissipate higher heat loads before receding onset. Since near-optimal pillar structures are examined, most wick structures can perform at the desired heat load without dry out.

The average evaporator superheats of non-drying ($q''_{dryout} > q''_{in} = 50$ W cm^{-2}) wick structures are presented in Figure 4.4. While keeping the aspect and pitch-to-pillar ratios constant, reducing the pillar diameter decreases the average evaporator superheat. Similarly, if the aspect ratio or the pitch-to-diameter ratio are reduced by keeping the pillar diameter constant, the average evaporator superheat diminishes for the same heat load.

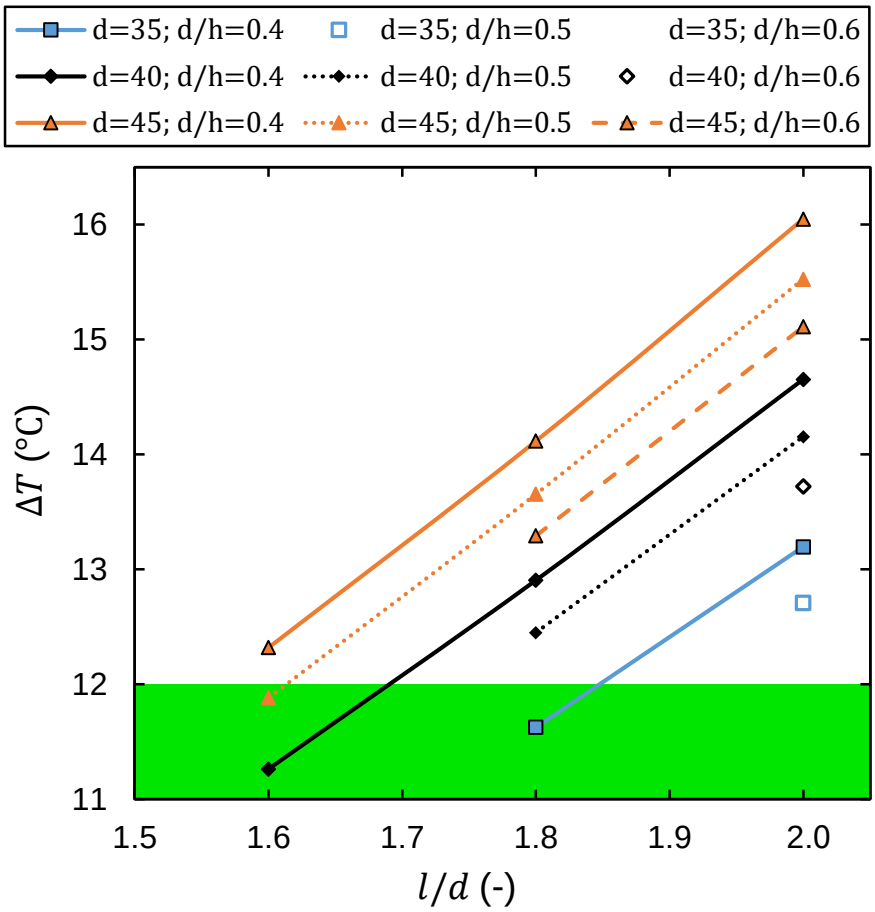

Figure 4.4: ΔT of non-drying pillar structures under 50 W cm^{-2} heat load. The green rectangle indicates the optimal wick structures for the design (q''_{in}=50 W cm^{-2}, t_s=650 μm, L=10 mm)

According to Figure 4.4, three wick structures (d=35 μm, l/d=1.8, d/h=0.4; d=40 μm, l/d=1.6, d/h=0.4; d=45 μm, l/d=1.6, d/h=0.5) in the green rectangle outperform the others with $\Delta T < 12$ °C. Choosing one of these three-wick structures according to the microfabrication constraints and dryout heat flux tolerances would be appropriate for the evaporator design.

In Figure 4.5, superheat variation on the base substrate is presented for one of the optimal wick structures ($d = 40\,\mu$m) at a heat load of $q''_{in} = 50\ \mathrm{W\,cm^{-2}}$. Although the average evaporator superheats is 11.3 °C for one of the optimized wick structures, there is a temperature variation of 4 °C along the wicking direction. The highest temperature is observed at the inlet due to the low heat transfer coefficients observed at high contact angles.

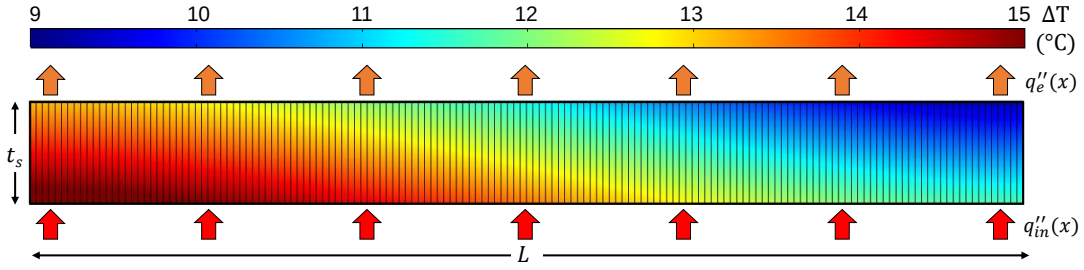

Figure 4.5: The superheat temperature contours within the base substrate under $50\ \mathrm{W\,cm^{-2}}$ heat load (d=40 μm, l/d=1.6, d/h=0.4, t_s=650 μm, L=10 mm).

4.3 Effect of Marangoni convection

In this section, in order to interpret the effect of Marangoni convection on these optimized geometries, the thermocapillary flow model is switched-on, and the simulations are repeated for the three optimal pillar structures. The average evaporator superheat predictions by both models (explained in Sec. 2.1.2 and Sec. 2.1.4) are compared at cell-level and device-level models. Since the look-up tables generated in the cell-level model are utilized to estimate ΔT_{av} in the device-level model, the ΔT and h_{eff} predictions at various contact angles are compared in the Figure 4.6 and Figure 4.7.

Although the effect of thermocapillary flow on h_{eff} is similar in all three devices at the same contact angles, the Marangoni effect on ΔT is slightly higher in the

wick structure with a diameter of 45 μm. Since the temperature gradient on the meniscus is lower due to the expanded thin-film area at low contact angles, the effect of thermocapillary flow on enhancing heat transfer coefficient is limited. On the other hand, as the evaporator temperature increases significantly at higher contact angles, the effect of Marangoni flow becomes more pronounced and reduces the evaporator temperature.

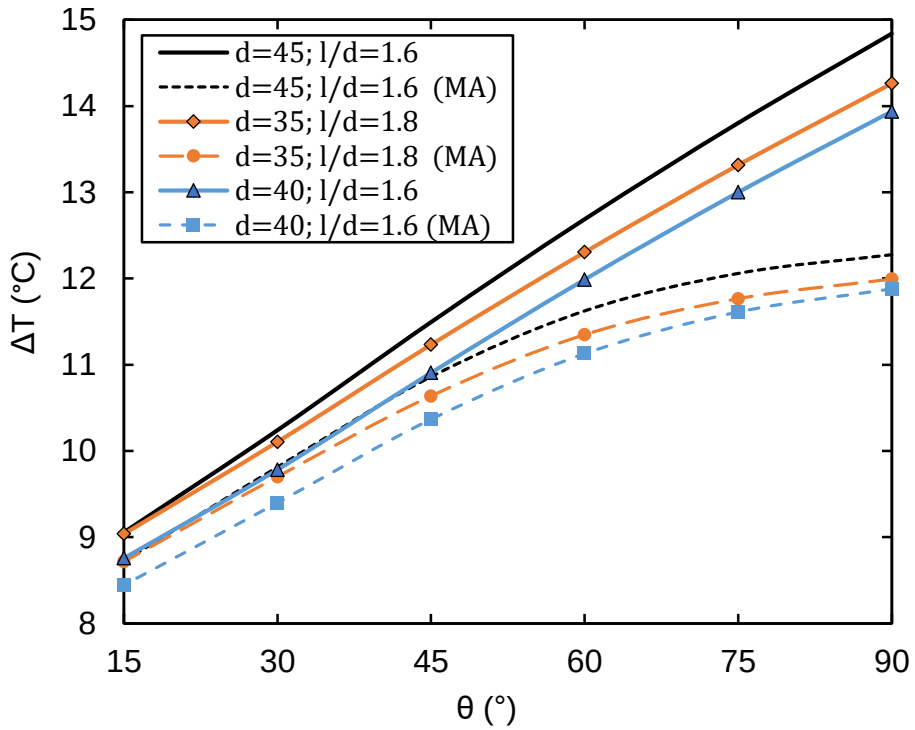

Figure 4.6: Comparison of ΔT prediction by non-isothermal and Marangoni model of three pillar configuration in cell-level model at various contact angles. At higher contact angles, the effect of Marangoni convection significantly increases, consequently, evaporator superheat decreases. ($q''_{in} = 50\,\mathrm{W\,cm^{-2}}$, MAC=0.4).

The average evaporator temperatures predicted at the device level and the percentage difference between the two models are demonstrated in Table 4.1 for the three pillar structures. Marangoni convection reduces average superheat substantially. Moreover, ΔT_{av} distinction between different devices is also reduced due to the enhanced Marangoni effect with higher evaporator superheat. In the device-level model, the increasing heat transfer coefficient along the wicking direction driven by variation of capillary pressure results in non-uniform evaporation, as discussed in the preceding

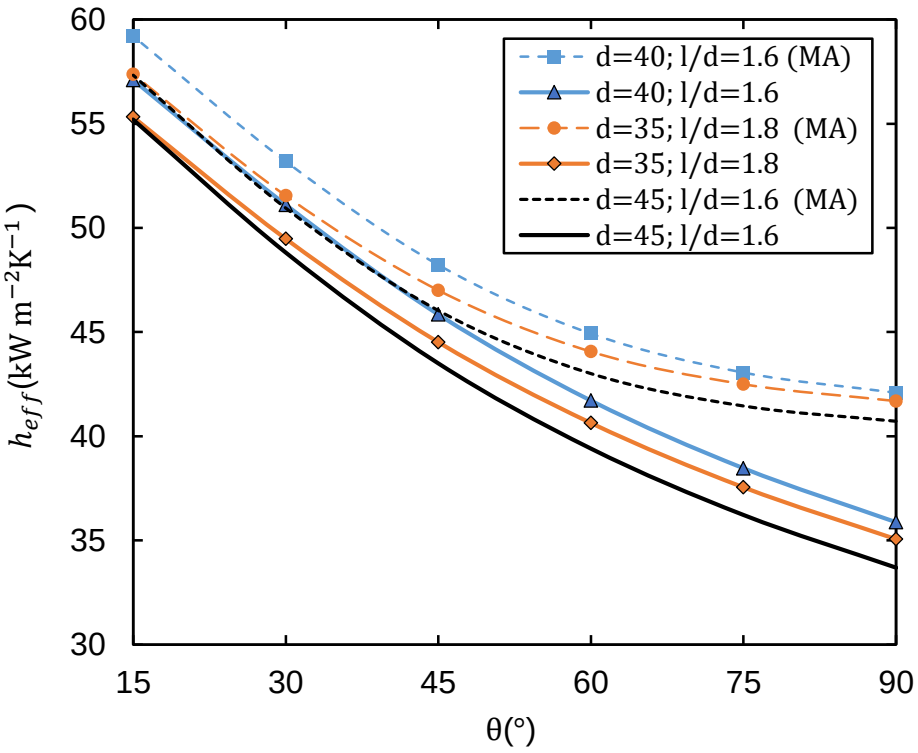

Figure 4.7: Comparison of h_{eff} prediction by non-isothermal and Marangoni models of three pillar configuration in cell-level model at various contact angles. At higher contact angles, the Marangoni convection significantly enhances heat transfer coefficient ($q''_{in} = 50\,\mathrm{W\,cm^{-2}}$, MAC=0.4).

sections. However, Marangoni convection significantly enhances the heat transfer coefficient at high contact angles. When Marangoni convection is switched-off, the model may mislead the engineers to calculate ΔT_{av} or specify the hot-spot region since thin-film evaporation and conduction within the substrate are not captured accurately. Therefore, it is essential to capture the Marangoni convection for optimized wick structures.

Considering the computational cost for the micropillar evaporator design, it would be appropriate to carry out the initial optimization studies with the simplified model (Sec. 2.1.2), then employ the Marangoni model (Sec. 2.1.4) for optimized geometries and high heat fluxes.

Table 4.1: Details of the optimal micropillar wick evaporators and comparison of average evaporator superheat predictions.

d	l/d	d/h	L	ΔT_{av}	ΔT_{av} (Ma)	Difference
μm	$-$	$-$	mm	°C	°C	%
35	1.8	0.4	10	11.6	10.6	9.1
40	1.6	0.4	10	11.3	10.3	8.6
45	1.6	0.5	10	11.9	10.7	10.0

CHAPTER 5

CONCLUSION AND SUGGESTIONS FOR FUTURE WORK

Evaporation from a micropillar wick evaporator is modeled by coupling the capillary liquid flow with energy transfer in both liquid and solid domains. Thermocapillary flow in micropillar evaporators is accounted for in the modeling for the first time in the literature. Predictions of the model are compared with a wide range of experimental results available in literature for water evaporation from micropillar evaporators, and excellent agreements are obtained. For the cases where the Ma number is relatively small, the effect of thermocapillarity on both dryout heat flux and average evaporator temperature is slight. However, when the Ma number is sufficiently high, thermocapillary convection sharply decreases the evaporator temperature by creating circulation beneath the liquid-vapor interface. This temperature reduction cannot be identified when thermocapillarity is not accounted for in the modeling. Therefore, the current study successfully reveals the role of Marangoni flow in the evaporation of water from micropillar wick evaporators. The current modeling approach can help researchers explore the relevant interfacial phenomena in the evaporation from the arrays of micro-scale surface structures and guide the engineers for the optimization of micro-post evaporators. An exemplary design study is carried out to guide the engineers in optimizing a micropillar evaporator, and the importance of Marangoni convection in the design is demonstrated. The effect of the Marangoni model on the effective heat transfer coefficient and prediction of average superheat is more conspicuous for the optimized designs with high dryout heat fluxes. The developed model that captures complex physics in thin-film evaporation can be expanded to simulate thin-film evaporation in capillary-driven passive heat spreaders such as heat pipes and vapor chambers.

REFERENCES

[1] G. E. Moore, "Cramming more components onto integrated circuits," *Electronics*, vol. 38, no. 8, p. 114, 1965.

[2] A. Bar-Cohen, M. Asheghi, T. J. Chainer, S. V. Garimella, K. Goodson, C. Gorle, and Y. Joshi, "The icecool fundamentals effort on evaporative cooling of microelectronics," *IEEE Trans. Compon. Packaging Manuf. Technol.*, vol. 11, no. 10, pp. 1546–1564, 2021.

[3] D. Li, G. S. Wu, W. Wang, D. Wang, Y. D .and Liu, D. C. Zhang, Y. F. Chen, G. P. Peterson, and R. Yang, "Enhancing flow boiling heat transfer in microchannels for thermal management with monolithically-integrated silicon nanowires," *Nano Lett.*, vol. 12, no. 7, pp. 3385–3390, 2012.

[4] D. Attinger, C. Frankiewicz, A. R. Betz, T. Schutzius, R. Ganguly, A. Das, C. J. Kim, and C. M. Megaridis, "Surface engineering for phase change heat transfer: A review," *MRS Energy & Sustainability*, vol. 1, 2014.

[5] Y. Akkus, C. T. Nguyen, A. T. Celebi, and A. Beskok, "A first look at the performance of nano-grooved heat pipes," *Int. J. Heat and Mass Tran.*, vol. 132, pp. 280–287, 2019.

[6] D. Ćoso, V. Srinivasan, M. C. Lu, J. Y. Chang, and A. Majumdar, "Enhanced heat transfer in biporous wicks in the thin liquid film evaporation and boiling regimes," *J. Heat Transf.*, vol. 134, no. 10, 2012.

[7] Y. Nam, S. Sharratt, C. Byon, S. J. Kim, and Y. S. Ju, "Fabrication and characterization of the capillary performance of superhydrophilic cu micropost arrays," *J. Microelectromech. Syst.*, vol. 19, pp. 581 – 588, 07 2010.

[8] R. Xiao, R. Enright, and E. N. Wang, "Prediction and optimization of liquid propagation in micropillar arrays," *Langmuir*, vol. 26, pp. 15070–5, 10 2010.

[9] R. Ranjan, A. Patel, S. V. Garimella, and J. Y. Murthy, "Wicking and thermal characteristics of micropillared structures for use in passive heat spreaders," *Int. J. Heat Mass Tran.*, vol. 55, no. 4, pp. 586–596, 2012.

[10] S. Ravi, D. Horner, and S. Moghaddam, "Monoporous micropillar wick structures, i-mass transport characteristics," *Appl. Therm. Eng.*, vol. 73, no. 1, pp. 1371–1377, 2014.

[11] Y. Zhu, D. Antao, Z. Lu, S. Somasundaram, T. Zhang, and E. N. Wang, "Prediction and characterization of dry-out heat flux in micropillar wick structures," *Langmuir*, vol. 32, no. 7, p. 1920—1927, 2016.

[12] G. Vaartstra, Z. Lu, and E. N. Wang, "Simultaneous prediction of dryout heat flux and local temperature for thin film evaporation in micropillar wicks," *Int. J. Heat Mass Tran.*, vol. 136, pp. 170–177, 2019.

[13] J. E. Drummond and M. Tahir, "Laminar viscous flow through regular arrays of parallel solid cylinders," *Int. J. Multiph. Flow*, vol. 10, pp. 515–540, 1984.

[14] B. R. Gebart, "Permeability of unidirectional reinforcements for rtm," *J. Compos. Mater.*, vol. 26, no. 8, pp. 1100–1133, 1992.

[15] M. P. Sobera and C. R. Kleijn, "Hydraulic permeability of ordered and disordered single-layer arrays of cylinders," *Phys. Rev. E*, vol. 74, p. 036301, 10 2006.

[16] A. Tamayol and M. Bahrami, "Transverse permeability of fibrous porous media," *Phys. Rev. E*, vol. 83, p. 046314, 04 2011.

[17] K. Yazdchi, S. Srivastava, and S. Luding, "Microstructural effects on the permeability of periodic fibrous porous media," *Int. J. Multiph. Flow* ., vol. 37, no. 8, pp. 956–966, 2011.

[18] D. Horner, S. Ravi, and S. Moghaddam, "Monoporous micropillar wick structures, ii-optimization & theoretical limits," *Appl. Therm. Eng.*, vol. 73, no. 1, pp. 1378–1386, 2014.

[19] R. S. Hale, R. Ranjan, and C. H. Hidrovo, "Capillary flow through rectangular micropillar arrays," *Int. J. Heat Mass Tran.*, vol. 75, pp. 710–717, 2014.

[20] R. S. Hale, R. T. Bonnecaze, and C. H. Hidrovo, "Optimization of capillary flow through square micropillar arrays," *Int. J. Multiphase Flow*, vol. 58, pp. 39–51, 2014.

[21] K. A. Brakke, "The surface evolver," *Exp. Math.*, vol. 1, no. 2, pp. 141–165, 1992.

[22] Y. Nam, S. Sharratt, G. Cha, and Y. S. Ju, "Characterization and modeling of the heat transfer performance of nanostructured cu micropost wicks," *J. Heat Transf.*, vol. 133, p. 101502, 10 2011.

[23] C. Byon and S. J. Kim, "The effect of meniscus on the permeability of micropost arrays," *J. Micromech. Microeng.*, vol. 21, p. 115011, 10 2011.

[24] A. S. Sangani and A. Acrivos, "Slow flow past periodic arrays of cylinders with application to heat transfer," *Int. J. Multiph. Flow*, vol. 8, no. 3, pp. 193–206, 1982.

[25] A. Tamayol and M. Bahrami, "Analytical determination of viscous permeability of fibrous porous media," *Int. J. Heat Mass Tran.*, vol. 52, no. 9, pp. 2407–2414, 2009.

[26] N. Srivastava, C. Din, A. Judson, N. C. MacDonald, and C. D. Meinhart, "A unified scaling model for flow through a lattice of microfabricated posts," *Lab on a chip*, vol. 10, pp. 1148–52, 05 2010.

[27] C. Zhang, "Analytical and experimental investigation of capillary forces induced by nanopillars for thermal management applications," *The Uni. of Texas at Austin*, 05 2010.

[28] R. Ranjan, J. Y. Murthy, and S. V. Garimella, "Analysis of the wicking and thin-film evaporation characteristics of microstructures," *J. Heat Transf.*, vol. 131, p. 101001, 2009.

[29] R. Ranjan, J. Y. Murthy, and S. V. Garimella, "A microscale model for thin-film evaporation in capillary wick structures," *Int. J. Heat Mass Tran.*, vol. 54, no. 1, pp. 169–179, 2011.

[30] N. Farokhnia, P. Irajizad, S. M. Sajadi, and H. Ghasemi, "Rational micro/nanostructuring for thin-film evaporation," *J. Phys. Chem. C*, vol. 120, pp. 8742–8750, 2016.

[31] K. Montazeri, H. Lee, and Y. Won, "Microscopic analysis of thin-film evaporation on spherical pore surfaces," *Int. J. Heat Mass Tran.*, vol. 122, pp. 59–68, 02 2018.

[32] M. Bongarala, H. Hu, J. Weibel, and S. V. Garimella, "A figure of merit to characterize the efficacy of evaporation from porous microstructured surfaces," *Int. J. Heat Mass Tran.*, vol. 182, p. 121964, 01 2022.

[33] S. Adera, D. Antao, R. Raj, and E. N. Wang, "Design of micropillar wicks for thin-film evaporation," *Int. J. Heat Mass Tran.*, vol. 101, pp. 280–294, 10 2016.

[34] R. W. Schrage, *A Theoretical Study of Interphase Mass Transfer*. Columbia University Press, New York, 1953.

[35] M. Wei, B. He, Q. Liang, S. Somasundaram, C. S. Tan, and E. N. Wang, "Optimization and thermal characterization of uniform silicon micropillar based evaporators," *Int. J. Heat Mass Tran.*, vol. 127, pp. 51–60, 2018.

[36] S. Somasundaram, Y. Zhu, Z. Lu, S. Adera, H. Bin, W. Mengyao, S. T. Tan, and E. N. Wang, "Thermal design optimization of evaporator micropillar wicks," *Int. J. Therm. Sci.*, vol. 134, pp. 179–187, 2018.

[37] H. Ghasemi and C. A. Ward, "Energy transport by thermocapillary convection during sessile-water-droplet evaporation," *Phys. Rev. Lett.*, vol. 105, no. 13, p. 136102, 2010.

[38] Y. Kita, A. Askounis, M. Kohno, Y. Takata, J. Kim, and K. Sefiane, "Induction of marangoni convection in pure water drops," *Appl. Phys. Lett.*, vol. 109, no. 17, p. 171602, 2016.

[39] O. Akdag, Y. Akkus, B. Cetin, and Z. Dursunkaya, "Interplay of transport mechanisms during the evaporation of a pinned sessile water droplet," *Phys. Rev. Fluids*, vol. 6, p. 073605, 2021.

[40] J. R. Barber, “The effect of thermal distortion on constriction resistance,” *Int. J. Heat Mass Tran.*, vol. 14, no. 6, pp. 751–766, 1971.

[41] V. P. Carey, *Liquid-vapor Phase Change Phenomena*. Hemisphere Publishing House, New York, 1992.

[42] *COMSOL Multiphysics ® v. 5.6*. "www.comsol.com", COMSOL AB, Stockholm, Sweden.

[43] Y. Akkus, A. T. Gurer, and K. Bellur, “Drifting mass accommodation coefficients: in situ measurements from a steady state molecular dynamics setup,” *Nanosc. Microsc. Therm.*, vol. 25, no. 1, pp. 25–45, 2021.

[44] A. H. Persad and C. A. Ward, “Expressions for the evaporation and condensation coefficients in the hertz-knudsen relation,” *Chem. Rev.*, vol. 116, no. 14, pp. 7727–7767, 2016.

[45] H. Hu and R. G. Larson, “Analysis of the effects of marangoni stresses on the microflow in an evaporating sessile droplet,” *Langmuir*, vol. 21, no. 9, pp. 3972–3980, 2005.

[46] R. Marek and J. Straub, “Analysis of the evaporation coefficient and the condensation coefficient of water,” *Int. J. Heat Mass Tran.*, vol. 44, no. 1, pp. 39–53, 2001.

[47] G. Vaartstra, L. Zhang, Z. Lu, C. D. Díaz-Marín, J. C. Grossman, and E. N. Wang, “Capillary-fed, thin film evaporation devices,” *J. Appl. Phys.*, vol. 128, no. 13, p. 130901, 2020.

[48] T. Ishiyama, T. Yano, and S. Fujikawa, “Molecular dynamics study of kinetic boundary condition at an interface between argon vapor and its condensed phase,” *Phys. Fluids*, vol. 16, no. 8, pp. 2899–2906, 2004.

Appendix A

APPENDIX

A.1 Mesh Independence Study

This section presents the mesh independence study for the meniscus shape, liquid transport, heat transport, and thermocapillary flow simulations at the cell-level model. While the mesh is being refined, the corresponding change in the selected parameter together with the corresponding solution time are reported in Fig. A.1. The orange arrows on the plots indicate the chosen mesh for the model to obtain sufficiently accurate results with a low computational cost. Since the total number of degrees of freedom solved for (DOF= total number of nodes x dependent variables) depends on pillar dimensions, the equations solved in the problem, and the contact angle; simulations are conducted for relatively large pillar dimensions with a low contact angle ($d = 30\,\mu\mathrm{m}$, $l = 60\,\mu\mathrm{m}$, $h = 60\,\mu\mathrm{m}$, $\theta = 30^o$).

Properties of water at $25^{\circ}\mathrm{C}$ are utilized for mesh independence study. The periodic pressure difference is set to 15 Pa across a unit-cell during the flow modeling, and input heat flux is set to 60 $\mathrm{W\,cm^{-2}}$. It should be noted that the corresponding Marangoni number is sufficiently high to induce thermocapillary flow.

Default discretization settings of the COMSOL Multiphysics (P1-P1: first order for velocity and pressure) for laminar flow and quadratic Lagrange discretization for temperature are used in the solutions of this study. Increasing the discretization order does not sensibly affect the results but drastically increases the solution time. Therefore, the solutions in this study are assumed to be discretization and mesh independent.

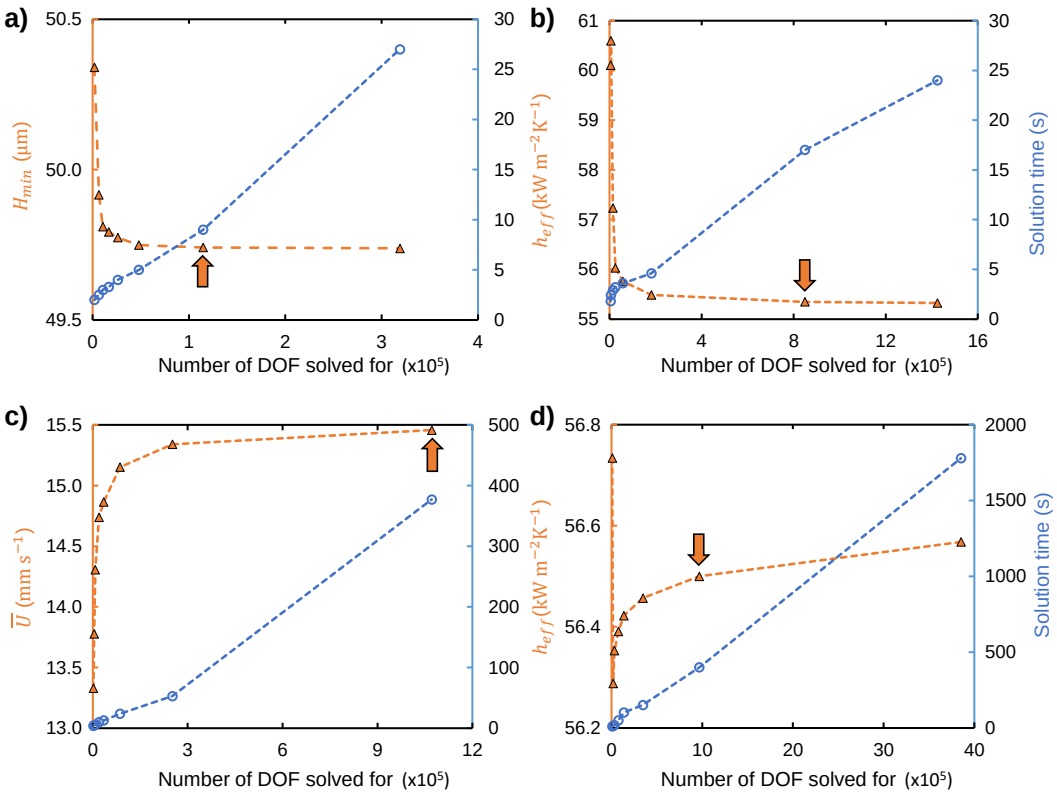

Figure A.1: Mesh independence study at the cell-level **a)** meniscus shape, **b)** energy transport, **c)** liquid transport, and **d)** thermocapillary flow simulations. Minimum meniscus height, average velocity, and effective heat transfer coefficient are investigated across the solution time.

A.2 Bi-directional Flow Model

Since the square wick structure utilized in the experiments conducted by Adera *et al.* [33] is in contact with the liquid from all sides, the current model is adapted to solve the bi-directional flow in the device-level model. Due to the isotropic wicking flow in lateral directions, only one-quarter of the evaporator is considered as the problem domain. A two-dimensional domain is modeled to solve Darcy's law problem in COMSOL Multiphysics [42], and permeability values are acquired from the cell-level models as a function of geometry and capillary pressure. Thin-film evaporation within the evaporator is modeled by the volumetric flow rate via point mass sources uniformly distributed over the domain. Applied heat flux is compensated by passive liquid propagation from the outer side of the domain.

The capillary pressure is set to zero at two inlet boundaries, and the symmetric boundary condition is utilized at the remaining boundaries. In Figure A.2a, the problem domain is demonstrated with wicking directions and corresponding boundary conditions. Resultant capillary pressure and velocity magnitude variations on Device-1 are shown in Figures A.2b and A.2c.

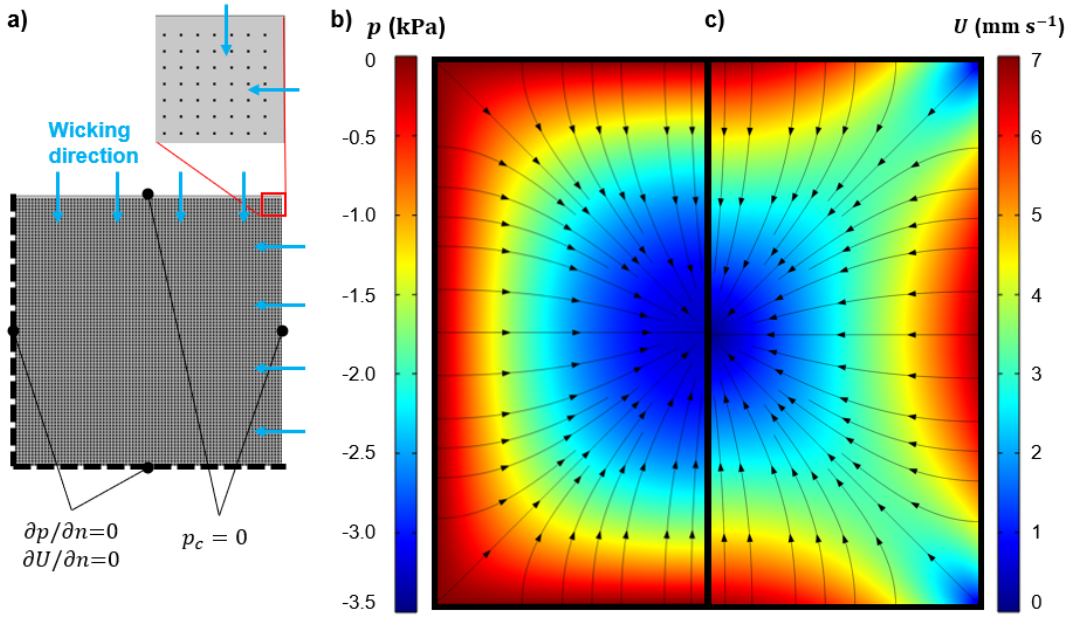

Figure A.2: **a)** Problem domain of bi-directional flow model, and the boundary conditions. **b)** Capillary pressure variation with superimposed streamlines and **c)** velocity magnitude distribution with superimposed streamlines on Device-1. The applied heat flux is 40 $\mathrm{W\,cm^{-2}}$ for the sample problem.